

Chapter 8

Simulation

Inaccurate prediction of Passive Magnetic Attitude Control (PMAC) performance has hindered the use of such systems for some satellite missions. The purpose of the software work is to develop a numerical simulation which accurately describes the response of a satellite using a PMAC system. Such a simulation could be used to predict the settling time of a satellite using a PMAC system. The settling time is considered the most important system characteristic as it allows for mission planning using predictive simulation. To this end, a simulation is developed and defined below in terms of its major components; this will allow future mission teams to use it for predictive mission requirements verification.

The simulation is built within the MATLAB[®] environment, which is used to numerically integrate the equations of motion. Models are defined for each environmental torque at low earth orbit. An orbit propagation method is defined because many environmental torques are dependent on satellite position. With the simulation components fully defined, analysis is performed to answer basic questions about the expectations of the simulation. Finally, the simulation output is shown given nominal input; the output is compared to the on-orbit data analyzed in Chapter 6.

We seek to understand the PMAC system behavior where possible, but here we do not aim to fully describe the underlying dynamics. Instead, the PMAC simulation development and testing given select initial inputs are described. Whenever possible, simulation results which shed light on the underlying dynamics are discussed. However, the scope of this research is limited to the simulation development and validation. Further testing given a wider variety of initial input may

be helpful in a deeper understanding of the general dynamics of a PMAC satellite.

8.1 Components

The attitude simulation is built from many components. Each component is defined in the subsections below. The reader should be able to recreate the simulation using the information described in this section.

8.1.1 Frames

There are three frames, or coordinate systems, used in the PMAC simulation. The first of these is the Earth Centered Inertial (ECI) frame. The ECI frame ${}^T\{X\ Y\ Z\}$ has its origin at the center of earth, with direction vectors defined as follows: ${}^T X$ lies in earth's equatorial plane and is parallel to the vernal equinox direction, ${}^T Z$ is parallel to the rotation axis of earth, and ${}^T Y$ is defined by the right-hand rule.

The second frame used in the PMAC simulation is the body frame ${}^B\{X\ Y\ Z\}$ of the spacecraft. The body frame is chosen to align with the principle inertia axes of the spacecraft. The body frame has its origin at the satellite center of mass with ${}^B X$ parallel to the REPTile collimator, ${}^B Z$ parallel to the satellite antenna, and ${}^B Y$ defined by the right-hand rule; Figure 4.3 shows the spacecraft body frame. The 3×3 matrix $[R]$ is defined to rotate an arbitrary vector \mathbf{v} from the inertial frame to the body frame:

$${}^B \mathbf{v} = [R] {}^T \mathbf{v}. \quad (8.1)$$

This rotation matrix will change at each step of the simulation as rotational dynamics change the attitude of the spacecraft relative to the inertial frame. More detail on the inertial to body frame rotation matrix is given in Section 8.1.2.

The final frame is the Earth Centered Earth Fixed (ECEF) frame which rotates with Earth. The ECEF frame ${}^E\{X\ Y\ Z\}$ has its origin at the center of earth with direction vectors defined as follows: ${}^E X$ lies in earth's equatorial plane and is parallel to the prime meridian ($0^\circ N$, $0^\circ E$), ${}^E Z$ is

parallel to the rotation axis of earth (90°N), and EY is defined by the right hand rule (0°N , 90°E). The conversion between the ECI and ECEF coordinate frames is not dependent on the satellite attitude; it is defined by the following rotation matrix:

$$\begin{bmatrix} X \\ Y \\ Z \end{bmatrix}_{\mathcal{E}} = \begin{bmatrix} \cos(\lambda_0 + \omega_E t) & \sin(\lambda_0 + \omega_E t) & 0 \\ -\sin(\lambda_0 + \omega_E t) & \cos(\lambda_0 + \omega_E t) & 0 \\ 0 & 0 & 1 \end{bmatrix} \begin{bmatrix} X \\ Y \\ Z \end{bmatrix}_{\mathcal{T}} \quad (8.2)$$

where λ_0 is the Greenwich Mean Sidereal Time (GMST) when the simulation starts, ω_E is the sidereal rotation rate of earth (rotation rate relative to fixed stars) and t is the time since simulation start. Figure 8.1 shows both the ECI and ECEF coordinate frames. The ECEF frame is useful because many inertial models are given in this frame.

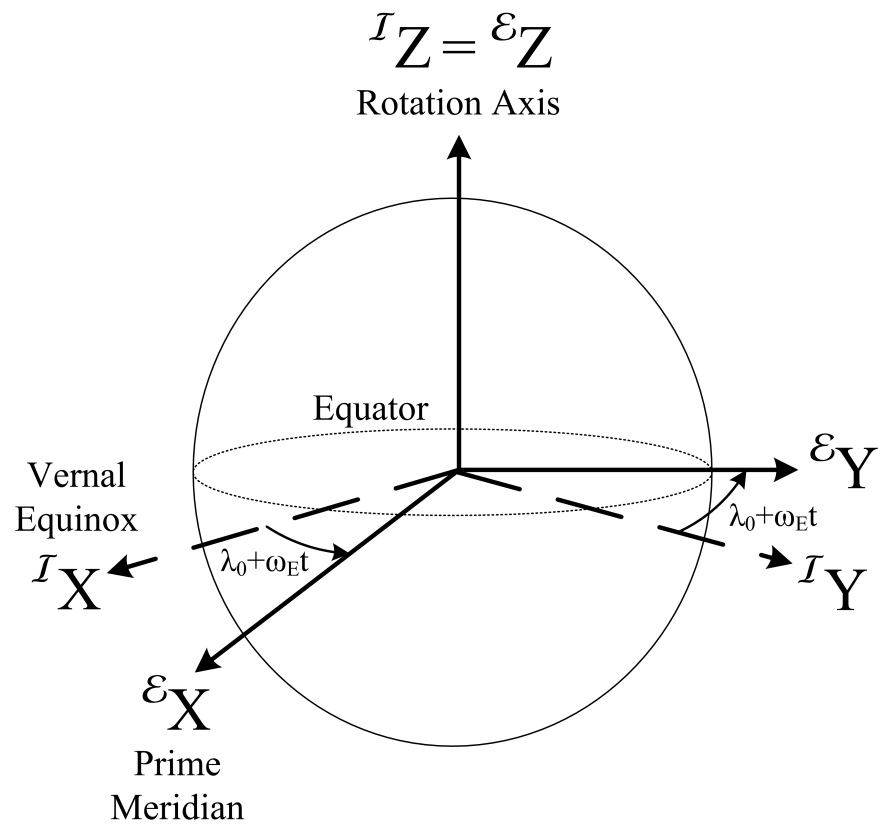
8.1.2 Attitude Parameters

The rotation matrix is useful for converting vectors from one frame to another. Also, it is simple to work with; the reverse rotation matrix (body to inertial) is found by simply transposing the original rotation matrix: $[R] = [R]_{\text{BI}} = [R]_{\text{IB}}^T$. However, the rotation matrix is a nine-dimensional representation of a three-dimensional rotation; six elements are redundant [65]. These redundant elements can lead to inaccurate modeling as rounding errors soften the constraints.

Three dimensional attitude parameters (such as Euler Angles) always contain a singularity in their kinematic differential equation at some specific attitude, making them undesirable for numerical integration purposes. A good compromise is the quaternion, a four-dimensional attitude parameterization with a single redundant parameter. The relation between the quaternion and the rotation matrix is given by [65]:

$$[R]_{\text{BI}} = \begin{bmatrix} q_0^2 + q_1^2 + q_2^2 + q_3^2 & 2(q_1q_2 + q_0q_3) & 2(q_1q_3 - q_0q_2) \\ 2(q_1q_2 - q_0q_3) & q_0^2 - q_1^2 + q_2^2 - q_3^2 & 2(q_2q_3 + q_0q_1) \\ 2(q_1q_3 + q_0q_2) & 2(q_2q_3 - q_0q_1) & q_0^2 - q_1^2 - q_2^2 + q_3^2 \end{bmatrix} \quad (8.3)$$

Figure 8.1: The ECEF and ECI coordinate frames are shown.



where q_0 is the scalar part of the quaternion and $[q_1 \ q_2 \ q_3]^T$ is the vector part. The quaternion has a single constraint: $q_0^2 + q_1^2 + q_2^2 + q_3^2 = 1$. This constraint is easily satisfied by normalization at a certain interval. The simulation developed in this chapter re-normalizes the quaternion every 100 integration steps; this frequency is chosen as a balance between computational performance and error tolerance.

8.1.3 Equations of Motion

The core of the simulation is Euler's rotational equation of motion (Equation 2.1). However, this equation cannot be integrated alone; it must be combined with a kinematic differential equation which defines the relationship between the angular velocity and the rate of change of the attitude parameters. As such, the kinematic differential equation is dependent on the parameter set used to represent the attitude. The kinematic differential equation for quaternions is given as [65]:

$$\begin{bmatrix} \dot{q}_0 \\ \dot{q}_1 \\ \dot{q}_2 \\ \dot{q}_3 \end{bmatrix} = \begin{bmatrix} q_0 & -q_1 & -q_2 & -q_3 \\ q_1 & q_0 & -q_3 & q_2 \\ q_2 & q_3 & q_0 & -q_1 \\ q_3 & -q_2 & q_1 & q_0 \end{bmatrix} \begin{bmatrix} 0 \\ \omega_1 \\ \omega_2 \\ \omega_3 \end{bmatrix} \quad (8.4)$$

where the scalar-first quaternion convention is used.

8.1.4 Orbit Propagation

The PMAC simulation assumes that the satellite rotation and translation are not coupled; thus the attitude has no effect on the orbit of the spacecraft. This assumption results in inertial satellite position and velocity vectors which are directly related to the orbit elements at some epoch and time relative to this epoch. These inertial position and velocity vectors are used as inputs for the inertial models described in Section 8.1.5.

The CSSWE orbit mean elements at a given epoch are provided by a Two-Line Element (TLE) set. This TLE is provided by the Joint Space Operations Center (JSpOC) for use with

the CSSWE mission. The orbit elements contained within the TLE make specific assumptions about the orbit and are designed to be propagated using only select orbit propagation schemes [35]. The PMAC simulation uses an updated version of the SGP4 propagator [79] designed for TLE propagation; the same method is used to calculate the CSSWE position for real-time on-orbit operations.

The first usable TLE has an epoch over ten days after launch, as shown in Figure 4.8. The datasets shown later in this chapter simulate the first ten days on orbit and thus use one TLE over this time period. Although the TLE is most accurate close to the epoch, no other position estimate is available for the early mission and on-orbit telemetry has shown the TLE-based position to be accurate to at least ± 6 seconds (Figure 4.8). Using one TLE throughout the simulation has the advantage of avoiding discontinuities in satellite position and velocity which would be generated during the switch from one TLE to the next.

8.1.5 Inertial Vector Models

The simulation uses two models to generate the inertial vectors for both magnetic field and sun position. The magnetic field model is solely dependent on satellite position in the ECEF frame, while the sun position model is solely dependent on date. Both are defined below.

8.1.5.1 International Geomagnetic Reference Field Model

The PMAC simulation uses the eleventh generation International Geomagnetic Reference Field (IGRF-11) model [23] to generate the inertial magnetic field vector. The IGRF is based on empirical measurements and is widely used as a magnetic field model for many applications. The IGRF represents the magnetic flux density as the negative gradient of a scalar potential function ($\mathbf{B} = -\nabla V$) which is defined by a spherical harmonics series which is set by a maximum of 195 coefficients (order 13). These coefficients are updated every five years; the latest epoch is 2010. The model also predicts some coefficients for the next five years after the latest epoch at one year intervals; 80 coefficients are predicted (order 8). The model sets coefficients for times between the

prediction year epochs using linear interpolation.

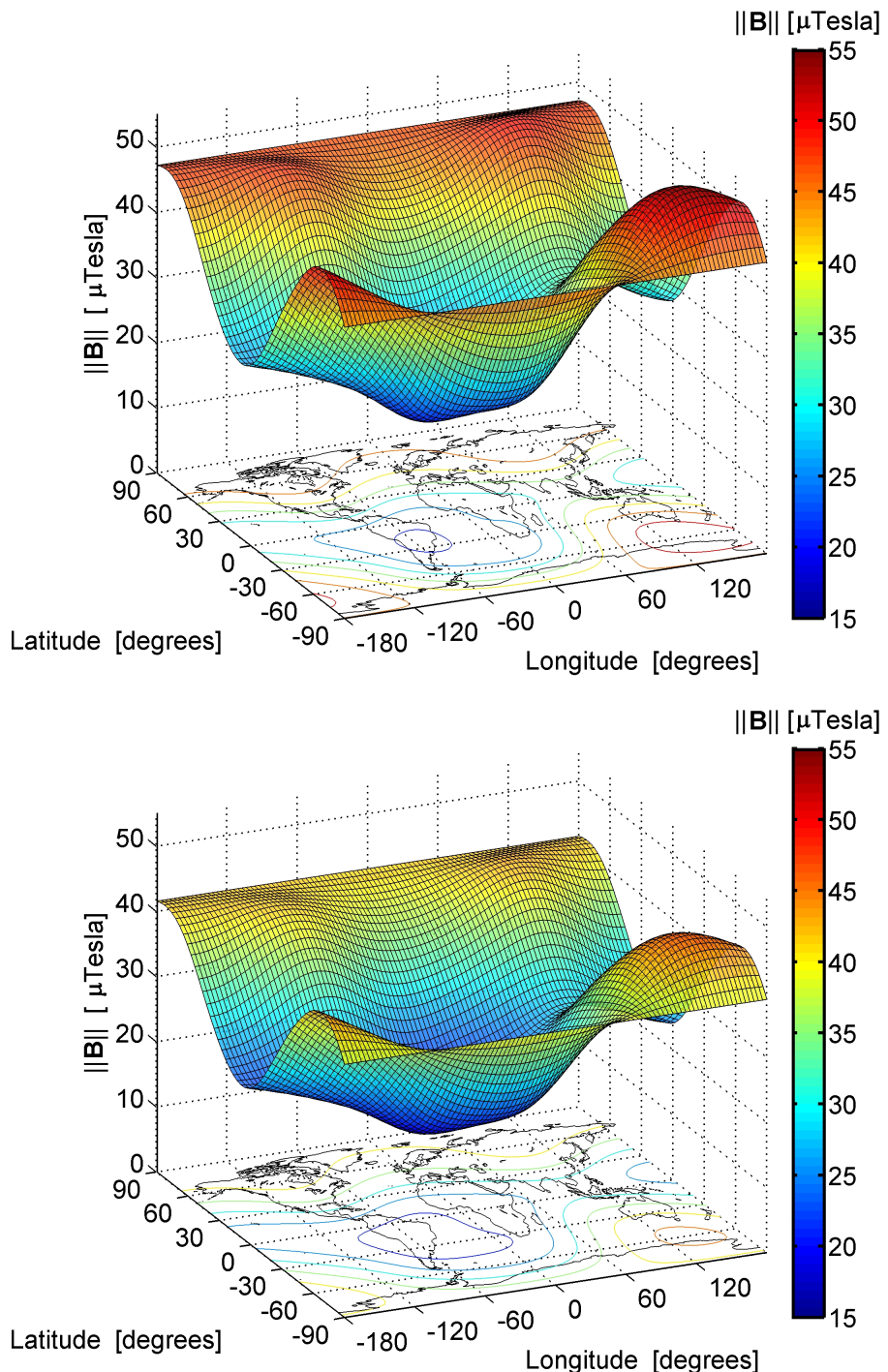
The IGRF is designed to provide an estimate of the magnetic field at the earth surface and above due to magnetic materials below the surface; it does not take into account variation due to space-based activity such as solar rotation, ionospheric currents, and geomagnetic storms. However, it does account for internal variations in the magnetic flux density which take place over a timespan of months to decades; this “secular variation” accounts for a global surface-level root mean squared magnitude change of about 80nT per year [6]. The IGRF-11 model predictions (for years after the 2010 epoch) of the core-based magnetic field are estimated to possess errors of up to 20nT per year [23]. Using the IGRF to model the inertial magnetic field experienced by a satellite can lead to higher errors, as discussed in Section 4.3.2.3.

Figure 8.2 shows the global magnetic flux density magnitude at altitudes of 450km and 770km (the extremes of the CSSWE orbit) as generated using the IGRF model with the 2012 predictive coefficients. This figure shows the range of magnetic flux densities which are used in the attitude simulation at various positions on-orbit. The CSSWE orbit experiences magnetic flux density magnitudes ranging from $17.6\mu\text{T}$ to $52.3\mu\text{T}$.

8.1.5.2 Inertial Sun Vector Model

The inertial sun position model is calculated using the method defined by Vallado [77]. A simplified version of the method which calculates the ECI frame unit vector from the center of earth to the sun ${}^T\hat{\mathbf{s}}$ is shown below:

Figure 8.2: Earth global magnetic flux density magnitude at altitudes of 450km (top) and 770km (bottom) as calculated using the eleventh-generation International Geomagnetic Reference Field (IGRF-11) model with the 2012 predictive coefficients.



$$T_{\text{UT1}} = \frac{JD_{\text{UT1}} - 2,451,545.0}{36,525} \quad (8.5)$$

$$\lambda_{M_{\text{sun}}} = 280.460\,618\,4 + 36,000.770\,053\,61 T_{\text{UT1}} \quad (8.6)$$

$$M_{\text{sun}} = 357.527\,723\,3 + 35,999.050\,34 T_{\text{UT1}} \quad (8.7)$$

$$\lambda_{\text{ecliptic}} = \lambda_{M_{\text{sun}}} + 1.914\,666\,471 \sin(M_{\text{sun}}) + 0.918\,994\,643 \sin(2M_{\text{sun}}) \quad (8.8)$$

$$\varepsilon = 23.439\,291 - 0.013\,004\,2 T_{\text{UT1}} \quad (8.9)$$

$$\hat{\mathbf{s}}^I = \begin{bmatrix} \cos \lambda_{\text{ecliptic}} \\ \cos \varepsilon \sin \lambda_{\text{ecliptic}} \\ \sin \varepsilon \sin \lambda_{\text{ecliptic}} \end{bmatrix} \quad (8.10)$$

where JD_{UT1} is the Julian Date, T_{UT1} is the number of centuries since the epoch, $\lambda_{M_{\text{sun}}}$ is the mean longitude of the Sun, M_{sun} is the mean anomaly of the Sun, $\lambda_{\text{ecliptic}}$ is the ecliptic longitude of the Sun, and ε is the obliquity of the ecliptic. All angles ($\lambda_{M_{\text{sun}}}$, M_{sun} , $\lambda_{\text{ecliptic}}$, and ε) are in units of degrees. This method is valid from 1950 to 2050 and is accurate to 0.01° [77]. It is not necessary to convert the unit vector from earth to the sun $\hat{\mathbf{s}}^I$ to the unit vector from the satellite to the sun; for a satellite at 1000km altitude, the angular difference between the center of the earth and the satellite position when perpendicular to the earth-sun vector (maximum error) is 0.0024° which is less than the 0.01° accuracy of the model.

It is useful to denote times at which the satellite is in eclipse. The simulation uses the method described by Kelso [41], outlined below. First, define the angular radii of the earth and sun as seen by the satellite:

$$\theta_E = \sin^{-1} \left(\frac{R_E}{\rho_E} \right) \quad (8.11)$$

$$\theta_S = \sin^{-1} \left(\frac{R_S}{\rho_S} \right)$$

where R_E and R_S are the true radii of the earth and sun, respectively and ρ_E and ρ_S are the distances from the satellite to the earth and sun, respectively. Next, the angle from the center of

the earth and the center of the sun (as seen by the satellite) is calculated as:

$$\theta_{ES} = \cos^{-1} (\mathbf{\hat{\rho}}_E \cdot \mathbf{\hat{\rho}}_S) \quad (8.12)$$

where $\mathbf{\hat{\rho}}_E$ is the body-frame unit vector from the satellite to earth and $\mathbf{\hat{\rho}}_S$ is the body-frame unit vector from the satellite to the sun. The earth-sun angle is used to determine when the sun is fully or partially eclipsed by the earth as shown below. Note that these equalities are only true when the earth appears larger than the sun (true for all satellite orbits within the moon's orbit):

$$\text{full eclipse (umbral):} \quad \theta_{ES} < \theta_E - \theta_S \quad (8.13)$$

$$\text{partial eclipse (penumbral):} \quad |\theta_E - \theta_S| < \theta_{ES} < \theta_E + \theta_S.$$

8.1.6 External Torque Estimation

A PMAC system relies upon two external torques for control: bar magnet and hysteresis torque. Other external torques are present due to the interaction of the spacecraft and the local environment: gravity gradient, aerodynamic (drag), solar pressure, magnetic residual, and eddy current. Each of these torques is described and modeled in the body frame for inclusion in Equation 2.1. The total external torque is simply:

$$\mathbf{L} = \mathbf{L}_B + \mathbf{L}_H + \mathbf{L}_G + \mathbf{L}_D + \mathbf{L}_{SP} + \mathbf{L}_R + \mathbf{L}_{EC} \quad (8.14)$$

8.1.6.1 Bar Magnet Torque

The bar magnet torque vector is given by Equation 2.6, repeated below.

$$\mathbf{L}_B = \mathbf{m}_{\text{bar}} \times \mathbf{B} \quad (2.6)$$

Note that there may be a large difference in the manufacturer-quoted value of bar magnet magnetic moment versus the true magnetic moment of the bar magnet \mathbf{m}_{bar} (see Section 7.2). The

local magnetic flux density \mathbf{B} is given by the IGRF model (see Section 8.1.5.1).

8.1.6.2 Hysteresis Torque

The hysteresis torque is the most difficult torque to model in the PMAC simulation due to the non-linear relationship between the local magnetizing field due to earth and the induced magnetization within the rod. Many models exist to attempt to predict this relationship; three such models are investigated in this research. As with the bar magnet torque, the IGRF model is used to calculate the local magnetic flux density vector \mathbf{B} . The component of the magnetizing field $\mathbf{H} = \mathbf{B}/\mu_0$ parallel to each hysteresis rod at the current time step is used as the applied field input to the hysteresis model. The component of the vector derivative of the magnetizing field as seen in the body frame $\frac{B_d}{dt}H$ is used as an input for each of the investigated hysteresis models. The component is calculated as $\frac{B_d}{dt}H = (\frac{B_d}{dt}\mathbf{H}) \cdot \hat{\mathbf{n}}_{\text{rod}}$ where $\hat{\mathbf{n}}_{\text{rod}}$ is a unit vector describing the orientation of the hysteresis rod.

Each model seeks to represent the average induced magnetic flux density parallel to the rod. Equation 2.7 converts the average parallel magnetizing field within the rod into the magnetic moment parallel to the hysteresis rod m_{hyst} at the current time step. The vector magnetic moment is calculated using $\mathbf{m}_{\text{hyst}} = m_{\text{hyst}}\hat{\mathbf{n}}_{\text{rod}}$. The torque provided by the hysteresis rods is then given by the magnetic torque equation:

$$\mathbf{L}_H = \mathbf{m}_{\text{hyst}} \times \mathbf{B} \quad (8.15)$$

8.1.6.3 Parallelogram Model

The parallelogram hysteresis model is the simplest and easiest model to implement [47] [61]. It is defined by a parallelogram that: intersects the y-axis at $\pm B_r$, intersects the x-axis at $\pm H_c$, and has a maximum absolute B-field output of B_s . The top curve is used when the magnetizing field derivative $\frac{B_d}{dt}H < 0$, while the bottom curve is used when $\frac{B_d}{dt}H \geq 0$. Thus, the output B is dependent only on H , $\frac{B_d}{dt}H$, H_c , B_r , and B_s and does not depend on cycle magnitude or frequency

or the previous magnetic flux density within the rod. The parallelogram model output is shown in blue in Figure 8.3.

8.1.6.4 Inverse Tangent Model

The inverse tangent hysteresis model [26] approximates the bounds of a typical hysteresis curve using the inverse tangent function. The model is defined as:

$$\begin{aligned}
 k &= \frac{1}{H_c} \tan\left(\frac{\pi B_r}{2B_s}\right) \\
 \text{if } \frac{B_d}{dt} H &\geq 0 : \\
 B &= \left(\frac{2B_s}{\pi}\right) \tan^{-1}(k(H - H_c)) \\
 \text{if } \frac{B_d}{dt} H &< 0 : \\
 B &= \left(\frac{2B_s}{\pi}\right) \tan^{-1}(k(H + H_c)).
 \end{aligned} \tag{8.16}$$

Again, the output B is dependent only on H , $\frac{B_d}{dt} H$, H_c , B_r , and B_s and does not depend on the magnetization cycle magnitude or frequency or the previous magnetic flux density within the rod. The inverse tangent model output is shown in green in Figure 8.3.

8.1.6.5 Flatley Model

The Flatley hysteresis model [26] is substantially different than the previous models, as it is defined in terms of a differential equation. While this adds complexity, the resultant loop is much more realistic as it can model minor hysteresis loops within the full loop as the hysteresis experiences lower cycle amplitudes. The Flatley model is defined as:

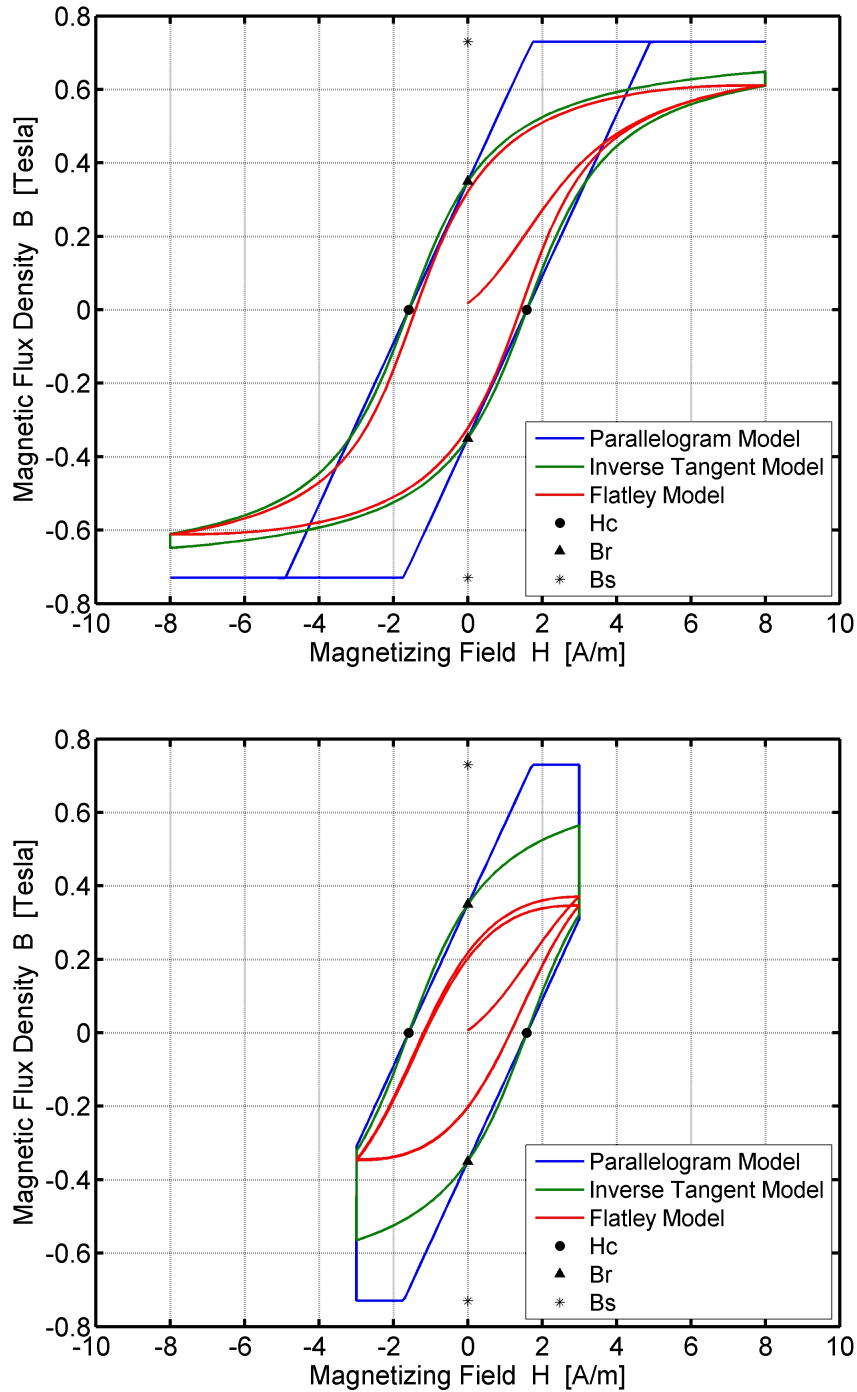
$$\begin{aligned}
k &= \frac{1}{H_c} \tan \left(\frac{\pi B_r}{2B_s} \right) \\
\text{if } \frac{\mathcal{B}_d}{dt} H &\geq 0 : \\
\dot{B} &= \left(q_0 + (1 - q_0) \left[\frac{1}{2H_c} \left(H - \frac{1}{k} \tan \left(\frac{\pi B}{2B_s} \right) + H_c \right) \right]^p \right) \left(\frac{2kB_s}{\pi} \right) \cos^2 \left(\frac{\pi B}{2B_s} \right) \left(\frac{\mathcal{B}_d}{dt} H \right) \\
\text{if } \frac{\mathcal{B}_d}{dt} H &< 0 : \\
\dot{B} &= \left(q_0 + (1 - q_0) \left[\frac{1}{2H_c} \left(H - \frac{1}{k} \tan \left(\frac{\pi B}{2B_s} \right) - H_c \right) \right]^p \right) \left(\frac{2kB_s}{\pi} \right) \cos^2 \left(\frac{\pi B}{2B_s} \right) \left(\frac{\mathcal{B}_d}{dt} H \right)
\end{aligned} \tag{8.17}$$

where q_0 and p are selectable constants which are tailored to fit a given empirical dataset. The model is found to perform best (most realistic over the wide range of magnetizing field cycle amplitudes) when $q_0 = 0$ and $p = 2$; these values have been used by other groups as well [58] [12]. The magnetic flux density time derivative \dot{B} is thus dependent on B , H , $\frac{\mathcal{B}_d}{dt} H$, H_c , B_r , and B_s . In practice, the Flatley model allows for the hysteresis rod magnetic flux densities to be integrated simultaneously with the attitude parameters and the angular velocity of the satellite. This means that the flux density is also dependent on the choice of numeric integrator, the simulation time step, and the hysteresis rod flux density of the previous integration step. Figure 8.3 shows a comparison of the output of the parallelogram, inverse tangent, and Flatley hysteresis models for two H-field cycles with amplitudes of ± 8 A/m and ± 3 A/m. The parallelogram and inverse tangent models are simply cutoff at lower cycle amplitudes, whereas the Flatley model actively adjusts to account for the changes in magnetizing field cycle amplitude.

The Flatley hysteresis model is chosen for this research because it was developed for numeric simulation of empirical datasets [26]. Also, the Flatley model has been used for a variety of past hysteresis dampening simulation [58], [43]. However, attempts to fit hysteresis measurement data using this model have shown its deficiencies (see Section 7.3).

The Flatley hysteresis model is numerically integrated and is not defined by two constant curves as the parallelogram and inverse tangent models are; as a result of this, some unique errors

Figure 8.3: Hysteresis loop output by three different hysteresis models with magnetizing field cycle amplitudes of ± 8 A/m (top) and ± 3 A/m (bottom). The parallelogram model (blue), inverse tangent (green), and Flatley (red) hysteresis models are shown. These loops were generated using closed magnetic circuit hysteresis parameters (see Table 7.2), two 1 Hz H -cycles, and a time step of 0.001s.



can occur. The Flatley model is designed to be bounded by the inverse tangent hysteresis model. Repeated simulation has shown that the Flatley-model-simulated hysteresis rod magnetic flux densities can sometimes exceed the bounds of the inverse tangent model for a time. In some extreme cases, the simulated rod magnetic flux density greatly exceeds the bounds of the inverse tangent model, corrupting the results of the PMAC simulation. This problem is resolved by checking the hysteresis rod magnetic flux density value after each simulation step. If the output exceeds the inverse tangent model bounds, the output is set to the top or bottom curve of the inverse tangent model, whichever is closer. This check prevents the erroneous behavior mentioned above.

8.1.6.6 Gravity Gradient Torque

The gravity gradient torque is given as follows [65]:

$${}^B\mathbf{L}_G = \left(\frac{3\mu_e}{R_c^5} \right) {}^B\mathbf{R}_c \times [I] {}^B\mathbf{R}_c \quad (8.18)$$

where μ_e is the earth gravitational parameter ($3.986 \cdot 10^5 \text{ km}^3\text{s}^{-2}$), ${}^B\mathbf{R}_c$ is the body-frame position vector from the center of earth to the center of mass of the spacecraft, and $[I]$ is, again, the spacecraft mass moment of inertia matrix. As shown, the gravity gradient torque is highest at low altitudes and is increased as the inertia matrix of the satellite becomes less symmetric. The torque acts to align the minimum inertia axis of a satellite with the nadir direction.

8.1.6.7 Aerodynamic Torque

The aerodynamic torque is calculated as follows [61]:

$${}^B\mathbf{L}_D = \frac{1}{2} \rho C_d ({}^B\mathbf{S} \cdot {}^B\mathbf{V}) ({}^B\mathbf{V} \times {}^B\mathbf{r}_d) \mathbf{e}_{\text{Error here.}} \quad (8.19)$$

where ρ is the density of the medium in which the spacecraft is traveling, C_d is the spacecraft coefficient of drag (assumed to be 2.4 for CSSWE), ${}^B\mathbf{S}$ is a vector defining the surface area of each of the body axes of the spacecraft ($[0.03 \ 0.03 \ 0.01]^T \text{ m}^2$ for a 3U CubeSat), ${}^B\mathbf{V}$ is the spacecraft

velocity vector in the body frame, and ${}^B\mathbf{r}_d$ is the body-frame position vector from the satellite center of mass to the geometric center (can be calculated using a solid model). The density ρ is the most difficult to calculate, as it can vary greatly depending on solar input and spacecraft altitude. The NRLMSISE-00 empirical model [59] is used by the simulation to estimate the atmospheric density for the position of the satellite at each time step. Daily and 81-day average F10.7 indices, as well as the average 3-hour ap index for the last 48 hours are all inputs to the NRLMSISE-00 model. The following assumed inputs are used: A daily F10.7 flux of $128.7 \cdot 10^{-22} \text{ J}\cdot\text{s}^{-1}\text{m}^{-2}\text{Hz}^{-1}$, an 81-day average F10.7 flux of $168.5 \cdot 10^{-22} \text{ J}\cdot\text{s}^{-1}\text{m}^{-2}\text{Hz}^{-1}$, and an average 3-hour ap index of 48. These inputs are defined in this way to simulate moderate solar activity.

8.1.6.8 Solar Pressure Torque

When the satellite is insolated (see Section 8.1.5.2), the force vector due to radiative pressure may be defined in the body frame as [78]:

$${}^B\mathbf{F}_{\text{SP}} = -P_S c_R \text{diag}({}^B\mathbf{S}) {}^B\hat{\mathbf{s}} \quad (8.20)$$

where P_S is the solar radiation pressure at earth (set to $4.5 \cdot 10^{-6} \text{ Pa}$ [36]), c_R is the coefficient of reflectivity of the satellite (assumed as 0.8), and ${}^B\hat{\mathbf{s}}$ is the body-frame unit vector from the earth to the sun. The torque vector due to solar pressure is thus:

$${}^B\mathbf{L}_{\text{SP}} = {}^B\mathbf{r}_d \times {}^B\mathbf{F}_{\text{SP}}. \quad (8.21)$$

8.1.6.9 Magnetic Residual Torque

The magnetic residual torque is due to undesired magnetism that may be present in the satellite. These magnetic residuals may be due to current loops, hard magnetic material in the satellite, or a misalignment of the PMAC bar magnet. The PMAC simulation models the residual magnetism as a constant magnetic moment vector in the body frame \mathbf{m}_{res} (set to $[-0.0059 \ -0.0083 \ 0.0004]^T \text{ A}\cdot\text{m}^2$), and the torque vector due to magnetic residual is calculated as:

$${}^B\mathbf{L}_R = \mathbf{m}_{\text{res}} \times {}^B\mathbf{B} \quad (8.22)$$

The chosen magnetic residual of CSSWE is based on a fit which minimizes the MEKF residuals (see Section 6.2.2); the residual is simply the difference between the fit and the assumed magnetic moment of the bar magnet \mathbf{m}_{bar} . However, future missions could determine the magnetic residual before flight using a method similar to the bar magnet measurement (see Section 7.2) if the satellite is measured in its flight configuration.

8.1.6.10 Eddy Current Torque

Eddy currents are generated when a conductor experiences a changing magnetic field. These circular currents induce their own magnetic field which can torque the satellite. The magnetic fields generated by eddy currents within rotating satellites are usually negligible compared to the local magnetic field; the simulation makes this assumption. Eddy currents can be generated in magnetic or non-magnetic conducting material but torques generated by currents within magnetic material are usually dwarfed by magnetization-based torques. The eddy current torque is partially based on area available for loops to form. Thus, it is assumed that the eddy currents generated by CSSWE are formed within the solid aluminum shell of the 3U CubeSat. The eddy current torque is given by [64]:

$$\mathbf{L}_{\text{EC}} = \sum_{i=1}^n (\mathbf{k}_i \cdot \hat{\mathbf{B}})(\boldsymbol{\omega} \times \mathbf{B}) \times \mathbf{B} \quad (8.23)$$

where there are n surface elements which generate eddy currents and \mathbf{k}_i is a vector constant set by a given surface element [30]:

$$\mathbf{k}_i = \frac{\pi}{4} \sigma_i r_i^3 A_i \hat{\mathbf{n}}_i \quad (8.24)$$

where σ_i is the conductivity of the surface element, r_i is the maximum circular loop radius that can form within the surface element, A_i is the area of the surface element, and $\hat{\mathbf{n}}_i$ is the unit vector

normal to the surface element. Note that currents will be generated in the same direction and add together instead of nullify (consider opposite sides of the same CubeSat); the sign of $\hat{\mathbf{n}}_i$ should reflect this behavior. The aluminum 3U solid shell of CSSWE was calculated to have $\mathbf{k}_1 = [147.3 \ 0 \ 0]^T$, $\mathbf{k}_2 = [0 \ 147.3 \ 0]^T$, and $\mathbf{k}_3 = [0 \ 0 \ 49.3]^T$, all in units of $A^2 \cdot s^3 \cdot m^2 \cdot kg^{-1}$.

8.1.7 Numeric Integrators

The choice of numeric integrator can have a great effect on the results of the simulation. In fact, much analysis is performed to select a numeric integrator and time step for the simulation (see Section 8.3). This subsection defines the numeric integrators which are considered for simulation use.

The most basic explicit numeric integrator is Euler's method; it uses the value and derivative at the current step to determine the value at the next step using a time step duration h :

$$y_{n+1} = y_n + h f(t_n, y_n) \quad (8.25)$$

$$t_{n+1} = t_n + h$$

where $f(t, y)$ is the rate of change of y at (t, y) . Decreasing the time step will yield better results, but Euler's method is often not the best choice for numerical integration. It is only accurate to first order. Also, it is possible that a higher-order integrator could yield more accurate results at a lower time step, thus saving computing resources. There are many higher-order explicit integrators; this research focuses on explicit Runge-Kutta integrators of order two through seven and the Lie Group Variational Integrator.

8.1.7.1 Runge-Kutta Integrators

Explicit Runge-Kutta methods of order greater than one calculate the next value using the current value, the current derivative, and the derivative at one or more points between each integration step. Explicit Runge-Kutta integration may be generalized as follows [34]:

$$y_{n+1} = y_n + h \sum_{i=1}^s b_i k_i \quad (8.26)$$

where

$$\begin{aligned} k_1 &= f(t_n, y_n) \\ k_2 &= f(t_n + c_2 h, y_n + a_{21} k_1) \\ k_3 &= f(t_n + c_3 h, y_n + a_{31} k_1 + a_{32} k_2) \\ &\vdots \\ k_s &= f(t_n + c_s h, y_n + a_{s1} k_1 + a_{s2} k_2 + \dots + a_{s,s-1} k_{s-1}) \end{aligned}$$

where the coefficients a_{ij} , b_i , and c_i are given by the Butcher tableau of the integrator in use. Appendix B explains the Butcher tableau and defines coefficients for integrators from order two to order seven.

This research investigates the performance of fixed time step integrators only; this limitation allows for improved data processing. Data from each simulation is saved at a rate of 1 Hz regardless of the integration time step; this reduces the size of save files and allows for direct comparison between datasets generated over a range of time steps. Adaptive step size Runge-Kutta methods do not possess these advantages.

8.1.7.2 Lie Group Variational Integrator

Researchers at the University of Michigan [44] have recently developed the Lie Group Variational Integrator (LGVI); it is designed to model long-term, low disturbance torques. LGVI is based on a discrete variational approach, and thus preserves the momentum of the system between time steps [45]. The Lie group integrator, created by Iserles et al. [37], is the basis of the LGVI. The Lie group numeric integrator uses the following integration rule:

$$[R]_{n+1} = \exp\left(-\frac{h}{2} ([\boldsymbol{\omega} \times]_n - [\boldsymbol{\omega} \times]_{n+1})\right) [R]_n. \quad (8.27)$$

where n is the current integration step, $n + 1$ is the next integration step, and h is the constant integration time step duration. Equation 8.27 gives the updated rotation matrix but it requires the new angular velocity $\boldsymbol{\omega}_{n+1}$ as an input. The new angular velocity could be calculated using a Runge-Kutta method to integrate Equation 2.1, but that could corrupt the momentum conservation which Equation 8.27 was developed to avoid. Lee et al. obtained the discrete Lie group variational numeric integrator rules by discretizing Hamilton's principle [45]:

$$\boldsymbol{\Pi}_{n+1} = [F]_n^T \boldsymbol{\Pi}_n + \frac{h}{2} [F]_n^T \mathbf{L}_n + \frac{h}{2} \mathbf{L}_{n+1} \quad (8.28)$$

$$h[\boldsymbol{\Pi} \times] + \frac{h^2}{2} [\mathbf{L} \times]_n = [F]_n [I_d] - [I_d] [F]_n^T \quad (8.29)$$

$$[R]_{n+1} = [R]_n [F]_n \quad (8.30)$$

where $\boldsymbol{\Pi} = [I]\boldsymbol{\omega}$ is the angular momentum vector, $[I_d]$ is a non-standard inertia matrix defined by $[I] = \text{tr}([I_d])[I_{3 \times 3}] - [I_d]$, and $[F]_n$ is the 3×3 rotation matrix defining the relative attitude between t_n and t_{n+1} . Thus, given the angular velocity and external torque vectors for the present time $(\boldsymbol{\omega}_n, \mathbf{L}_n)$, $[F]_n$ may be used to determine the state at the next step. However, in practice solving Equation 8.29 is not a trivial task because $[F]_n$ is a 3×3 matrix.

In order to solve for $[F]_n$, Lee introduces the 3×1 vector \mathbf{f}_n , defined by [45]:

$$\begin{aligned} [F]_n &= \exp [\mathbf{f} \times]_n \\ &= [I_{3 \times 3}] + \frac{\sin \|\mathbf{f}_n\|}{\|\mathbf{f}_n\|} [\mathbf{f} \times]_n + \frac{1 - \cos \|\mathbf{f}_n\|}{\|\mathbf{f}_n\|^2} [\mathbf{f} \times]_n^2. \end{aligned} \quad (8.31)$$

When Equation 8.31 is substituted into Equation 8.29 and the definition of a skew-symmetric matrix is used, it becomes:

$$h\boldsymbol{\Pi}_n + \frac{h^2}{2} \mathbf{L}_n = \frac{\sin \|\mathbf{f}_n\|}{\|\mathbf{f}_n\|} [I] \mathbf{f}_n + \frac{1 - \cos \|\mathbf{f}_n\|}{\|\mathbf{f}_n\|^2} \mathbf{f}_n \times [I] \mathbf{f}_n. \quad (8.32)$$

where Equation 8.32 is solved using Newton's method. Thus, given initial inputs, the PMAC simulation is time-marched continually using the following process [45]:

- (1) Determine \mathbf{f}_n using Newton's method to solve Equation 8.32 given $\boldsymbol{\omega}_n$ and \mathbf{L}_n

- (2) Determine $[F]_n$ using Equation 8.31 given \mathbf{f}_n
- (3) Determine $[R]_{n+1}$ using Equation 8.30 given $[R]_n$ and $[F]_n$
- (4) Determine \mathbf{L}_{n+1} using the models developed in Section 8.1.6 given $[R]_{n+1}$
- (5) Determine $\boldsymbol{\omega}_{n+1}$ using Equation 8.28 given $\boldsymbol{\omega}_n$, \mathbf{L}_n , \mathbf{L}_{n+1} , and $[F]_n$.

However, there are several drawbacks to using LGVI to integrate a PMAC simulation. It is difficult to include the hysteresis magnetizations as additional integration states. The LGVI estimates the attitude and angular velocity states after each integration step; the hysteresis magnetization integration is thus limited to Euler's method. It is possible to use a Runge-Kutta integrator between each LGVI integration step to obtain a higher-order estimate of the hysteresis magnetizations based on intermediate attitude estimates, but this has been found to greatly impact the processing time of the simulation. Instead, the simulation uses Euler's method to integrate the hysteresis magnetization when using LGVI for attitude integration, as has been done in the past [58] [44].

LGVI was developed to integrate rigid body dynamics when the external torque is dependent on attitude alone; it is not designed for torques which are dependent on angular velocity. The hysteresis torque is dependent on the body-frame time derivative of the magnetizing field (see Section 8.1.6.2); this is calculated using the transport theorem below [65]:

$$\begin{aligned} \frac{\mathcal{B}_d}{dt}(\mathbf{H}) &= \frac{\mathcal{I}_d}{dt}(\mathbf{H}) - \boldsymbol{\omega} \times \mathbf{H} \\ &= [R]^T \dot{\mathbf{H}} - \boldsymbol{\omega} \times [R]^T \mathbf{H} \end{aligned} \quad (8.33)$$

Thus, the hysteresis torque is dependent on the current rotation matrix and the current angular velocity. Previous work using the LGVI [44] assumes $\boldsymbol{\omega}_n \approx \boldsymbol{\omega}_{n+1}$ when calculating the hysteresis magnetization derivative; this work uses this approach for simulations using the LGVI with hysteresis torque. The explicit Runge-Kutta integration methods described in Section 8.1.7.1 do not possess the drawbacks listed above.

8.2 Considerations

It is helpful to briefly consider concepts of attitude dynamics which apply to a PMAC satellite. A basic grasp of these concepts will shed light on the simulation results presented later in this chapter.

8.2.1 Torque-Free Rigid Body Motion

A rigid body without any external torques acting upon it will behave according to gyroscopic motion alone (Equation 2.1 with $\mathbf{L} = 0$). With this special condition, the angular momentum vector $\mathbf{\Pi} = [I]\boldsymbol{\omega}$ is constant in the inertial frame and the magnitude of angular momentum is constant in any frame. Also, the total system energy (due to kinetic energy alone) is conserved. Taken together, this means the satellite motion is bounded by the intersection of the energy ellipsoid

$$T = \frac{1}{2}I_1\omega_1^2 + \frac{1}{2}I_2\omega_2^2 + \frac{1}{2}I_3\omega_3^2. \quad (8.34)$$

and the momentum ellipsoid

$$\Pi^2 = \mathbf{\Pi}^T \mathbf{\Pi} = I_1^2\omega_1^2 + I_2^2\omega_2^2 + I_3^2\omega_3^2. \quad (8.35)$$

The above equations may be manipulated such that the angular momentum of each axis Π_i are the independent coordinates; this results in a momentum sphere intersected by an energy ellipsoid. Figure 8.4 (modified from Fig. 4.6 of [65], used with permission) shows the momentum sphere and the energy ellipse assuming $I_1 > I_2 > I_3$ (the CSSWE inertia matrix follows this trend as well). When the system energy is at maximum, only rotation about the minimum inertia axis is possible ($\boldsymbol{\omega} = \pm\omega_3\hat{\mathbf{n}}_3$). However, if the system loses energy over time (due to structural flexing, hysteresis, etc.), the energy ellipsoid will shrink until the system energy is equivalent to motion about the intermediate axis. However, the motion is not necessarily about the intermediate axis because of the separatrix, the boundary between the high energy domain (wobble about $\pm\hat{\mathbf{n}}_3$) and the low energy domain (wobble about $\pm\hat{\mathbf{n}}_1$). The motion of a rigid body at the separatrix is inherently

chaotic as the energy ellipsoid intersects the momentum sphere in many places. As more energy is removed, the satellite will settle to a wobble about $\hat{\mathbf{n}}_1$ or $-\hat{\mathbf{n}}_1$; either is equally likely after motion along the separatrix. Continued damping will cause the motion to be solely about the major inertia axis ($\boldsymbol{\omega} = \pm\omega_1\hat{\mathbf{n}}_1$) [65].

Torque-free motion has important implications for a PMAC satellite. This is motion which every satellite experiences to some extent as it is present in the gyroscopic term of Equation 2.1. The extent to which a given satellite will “feel” the gyroscopic motion (and thus behave in this manner) may be examined by calculating the “gyroscopic torque” as follows:

$$\mathbf{L}_{GY} = -[\boldsymbol{\omega} \times][I]\boldsymbol{\omega}. \quad (8.36)$$

This “torque” (which a rigid body experiences even in the absence of external torque) is taken directly from Euler’s rotational equation of motion. If the gyroscopic torque \mathbf{L}_{GY} is much greater than the external torque \mathbf{L} then the rigid body will experience mainly torque-free motion. If the gyroscopic torque is much less than the external torque, torque free motion is not dominant. If the gyroscopic torques is similar in magnitude to the external torque, some combination of torqued and torque-free motion will result.

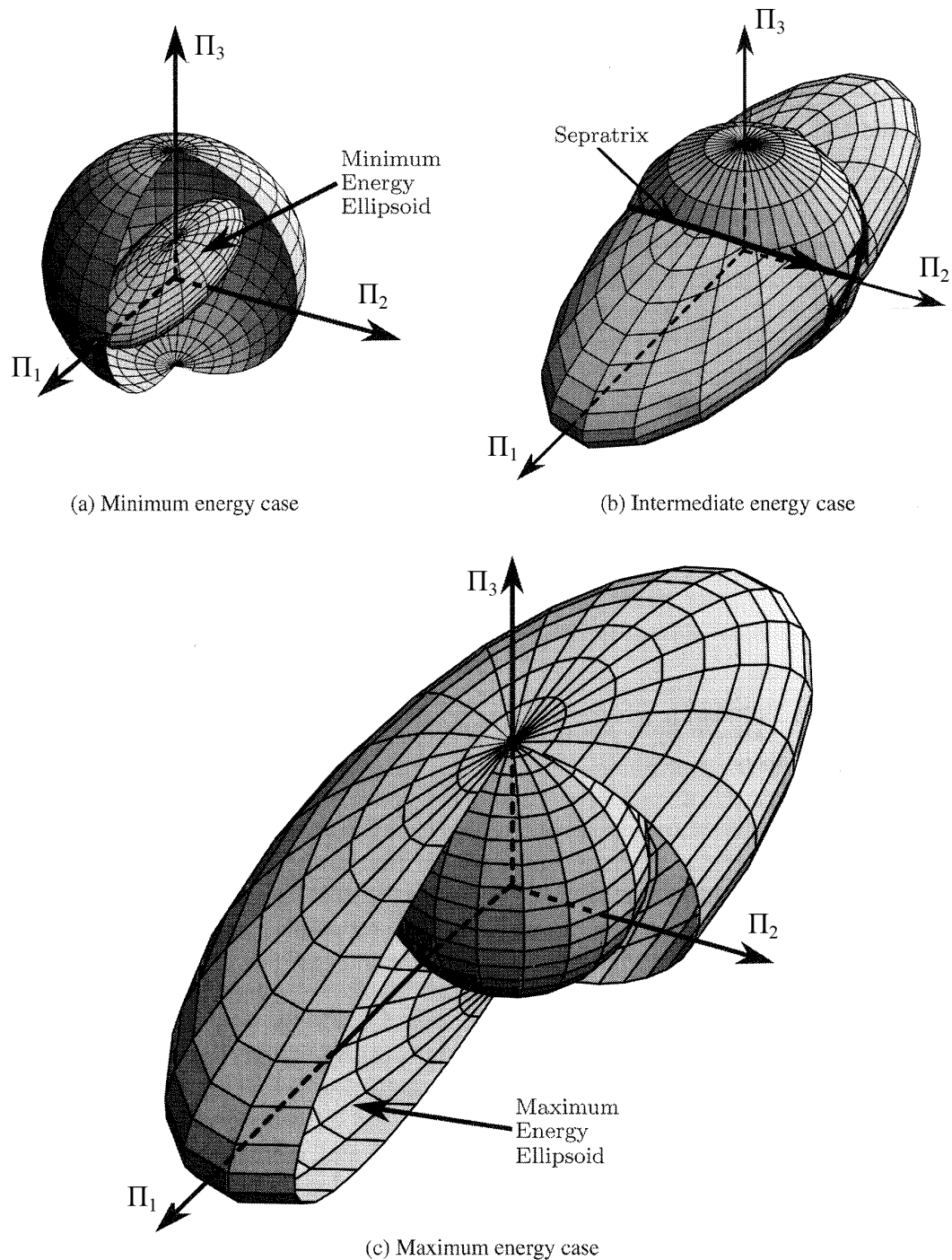
8.2.2 3D Pendulum Comparison

A satellite with a bar magnet in a constant magnetic field is dynamically equivalent to a rigid pendulum tethered at a distance to a fixed, frictionless point and acted upon by a constant gravitational acceleration. This special case is known as a 3D pendulum whose equations of motion are as follows [67]:

$$[I]\dot{\boldsymbol{\omega}} = -[\boldsymbol{\omega} \times][I]\boldsymbol{\omega} + \boldsymbol{\rho} \times m\mathbf{g} \quad (8.37)$$

where $\boldsymbol{\rho}$ is the distance vector from the pendulum center of mass to the pivot, m is the mass of the pendulum, and \mathbf{g} is the gravitational acceleration vector. Thus, the 3D pendulum $\boldsymbol{\rho}$ and $m\mathbf{g}$ are

Figure 8.4: Interactions of the momentum sphere and energy ellipse at (a) minimum energy, (b) intermediate energy, and (c) maximum energy conditions (modified from Fig. 4.6 of [65], used with permission).



analogous to the PMAC \mathbf{m}_{bar} and \mathbf{B} , respectively.

Because the equations of motion are numerically identical, conclusions drawn from previous studies of the 3D pendulum apply to the bar-magnet-only case of PMAC as well. What follows is a list of properties of the 3D pendulum which also apply to a PMAC satellite in certain conditions.

- (1) The 3D pendulum cannot be analytically solved [14]. If this is true of the PMAC bar-magnet-only case, it is also true of all other PMAC cases.
- (2) The 3D pendulum conserves the total energy of the system as well as the component of angular momentum about the axis parallel to mg (PMAC \mathbf{B}).
- (3) The system dynamics are unchanged by rotation about the axis parallel to ρ [67] (PMAC \mathbf{m}_{bar}).
- (4) The hanging equilibrium (with ρ parallel to mg and with the pendulum center of mass below the pivot) is Lyapunov stable [67]; initial states which are close to this point will remain close to this point. This is equivalent to a bar magnet which is aligned with the local magnetic field.
- (5) The inverted equilibrium (with ρ parallel to mg and with the pendulum center of mass above the pivot) is unstable [67]. This means that a small deviation from the equilibrium point could cause large changes in the state of the system. This is equivalent to a bar magnet anti-parallel to the local magnetic field.
- (6) Control in the form of $\mathbf{L} = \mathbf{u} \times mg$ (where \mathbf{u} is the control input) preserves the conservation of angular momentum along the axis parallel to mg [67]. This is analogous to PMAC hysteresis torque (Equation 8.15).

The instability described in point (5) means that the PMAC dynamics are sensitive when $\beta = 180^\circ$; this should not be confused with chaotic motion due to the separatrix. Point (6) is important as it implies that different dynamics are in effect when non-magnetic environmental torques are included in a simulation.

8.3 Simplified Simulation Analysis

This section seeks to answer two major questions:

- (1) Can a simulation be used to represent PMAC dynamics? If so, to what extent?
- (2) If a simulation can be used to represent PMAC dynamics, what integrator and time step should be used to ensure accurate output?

A simplified simulation is developed to answer these questions at a reasonable computational cost. Because this simplified simulation maintains the key properties of the full simulation, it is assumed that the lessons learned can be applied to the full simulation. The assumptions and conditions of the simplified simulation are discussed before using the simulation for a variety of analysis. This study considers the LGVI and RK2-RK7 integrators as well as time step values of 1s, 0.1s, and 0.01s.

8.3.1 Description

A simplified simulation is developed in an attempt to understand the base properties of the full simulation. This simplified simulation can run much faster than the full simulation yet retains its key properties. The first simplification is an inertially-constant magnetizing field vector; this simulates a circular equatorial orbit if the earth has a perfect dipole magnetic field aligned with its poles with no offset. Second, when external torques are included in the model, only the gravitational gradient and solar pressure torques are included. The gravitational gradient assumes a constant inertial position of 450 km altitude above the surface of earth along $+^IY$. The solar pressure torque assumes a constant inertial unit vector from the earth to the sun ${}^I\hat{\mathbf{s}} = [-1 \ 0 \ 0]^T$. Together, these are the gravity gradient and solar pressure torques for a prograde orbit dawn crossing at autumnal equinox; these constant inertial values are chosen for simple application and visualization. With these assumptions, only the ECI and body frames are required.

Two sets of initial inputs are run; each set is run through a variety of analysis. Both sets use a satellite magnetic moment $\mathbf{m} = [0 \ 0 \ 0.55]^T \text{ A}\cdot\text{m}^2$ and the principal moment of inertia matrix

Table 8.1: Nominal inputs for the simplified simulation sets are shown below. The derived values of β angle and initial system energy are also shown.

Parameter	Unit	Set 1	Set 2
Constant magnetizing field vector ${}^T\mathbf{H}$	A/m	$[0 \ 0 \ 20]^T$	$[25.18 \ 2.76 \ -8.59]^T$
Initial 1-2-3 Euler angles EA ₁₂₃	deg	$[90 \ 0 \ 0]^T$	$[13.9 \ -71.6 \ 104.1]^T$
Initial angular velocity vector ω_0	deg/s	$[1 \ 1 \ 1]^T$	$[0.17 \ -0.97 \ 2.93]^T$
<i>(Derived Values)</i>			
Initial β angle	deg	90	178.1
Initial system energy	J	$7.46 \cdot 10^{-6}$	$2.82 \cdot 10^{-5}$

given in Section 4.2. Other parameters which define the hysteresis, gravity gradient, and solar pressure torques are given in Table 8.2.

The input values for both initial condition sets are defined in Table 8.1. The first set uses a 20 A/m constant magnetizing field and starts with the satellite perpendicular to the magnetic field and rotating at one degree per second in pitch, yaw, and roll. Initial input set two is defined by the CSSWE attitude and angular velocity as calculated by MEKF for September 14, 2012 at 00:59:48 UTC; this is eight minutes after PPOD deployment and shortly after the MEKF converges to an attitude solution (see Chapter 6).

8.3.2 Energy Conservation Analysis

The numeric integrator itself can cause the simulated system energy to drift over time. Although this behavior is undesired, every combination of numeric integrator and time step will have some energy drift; the key is to determine an acceptable level of this drift. Here the maximum allowable energy drift is set as the energy dissipated by a single ± 20 A/m cycle of one flight hysteresis rod over a 1000 hour simulation time; this duration (about 42 days) is considered the longest timespan over which the simulation will be used to calculate a settling time. Using the fitted hysteresis loop area shown in Table 7.2 and the volume of a single flight hysteresis rod, this amounts to a maximum allowable energy change of $3.3 \cdot 10^{-9}$ J over a 1000 hour simulation. It is assumed that energy differences below this threshold will have a negligible effect on the dynamics because

the rod-based energy loss will dominate the integrator-based energy drift.

The energy conservation of each integrator and time step is analyzed by running the simplified simulation for 1000 hours with a bar magnet only; no hysteresis, gravity gradient, or solar pressure torques are included. Ideally, a freely-floating bar magnet in a constant magnetic field will perfectly conserve the initial system energy as there are no dampening torques included in the simulation. Figure 8.5 shows the maximum energy drift of each integrator and time step combination over 1000 hours of simulation using input sets 1 and 2; an energy drift of zero is ideal. Input set 2 results in energy drifts as high as 100 times the level of input set 1. This may be due to motion near the instability point at $\beta = 180^\circ$, which is not seen by the dynamics when using input set 1. Also, set 2 has a higher initial energy than set 1. Due to computational cost, this analysis is not repeated for all possible initial inputs; instead set 2 is assumed to be the worst-case initial input. Thus, the integrator and time step combinations with output beyond the energy drift threshold are ruled out for use in the full simulation.

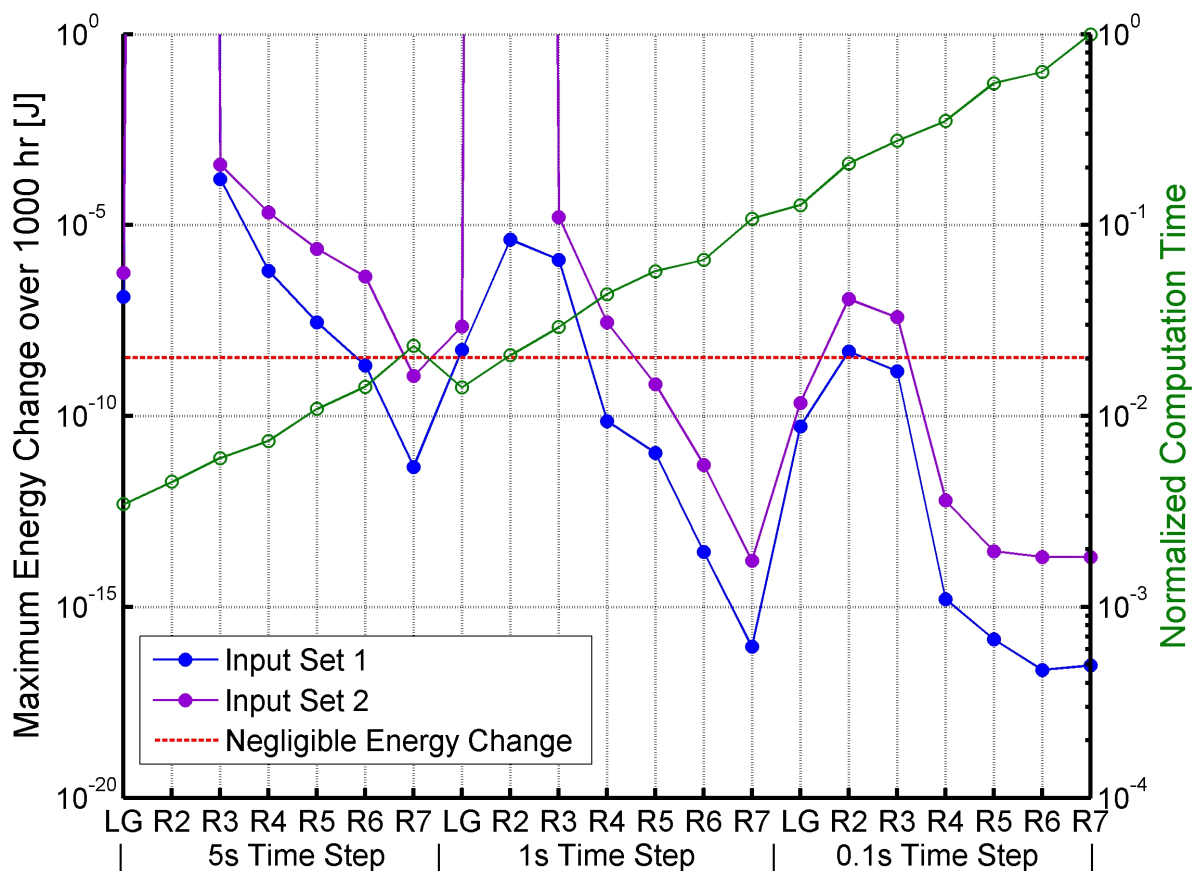
Although the LGVI is the quickest-running integrator for a given time step duration, its performance is often comparable to the RK4 at the same time step. Note that the higher-order integrators, when compared to the LGVI at a decreased time step, regularly show decreased energy drift at similar (or lower) computation times. This analysis is not in favor of using the LGVI for the attitude simulation as it is more complicated and more difficult to understand than Runge-Kutta methods while achieving similar performance.

8.3.3 Angular Error Analysis

The energy drift is not the only performance metric which can evaluate each integrator and time step combination; the beta angle error and the settling time error may also be used. However, the ideal beta angle and settling time are much more difficult to calculate than the bar-magnet-only system energy, which will ideally remain equal to the initial system energy. This problem is further complicated by the impossibility of an analytical solution for PMAC dynamics.

Here the approach is to compare each integrator and time step to the the highest-order,

Figure 8.5: The maximum energy change for each integrator and time step combination. The negligible energy change threshold of $3.3 \cdot 10^{-9} \text{ J}$ is denoted by the red dotted line. The normalized computation time of each simulation is also shown in green. The 0.01s time step is not shown due to the unreasonable computation times required to simulate 1000 hours.



lowest-time-step output, which is assumed to be “truth”. Figure 8.6 defines error relative to the RK7/0.01s output and shows the maximum beta angle error for simulations over a 30 hour duration using initial input sets 1 and 2. Three cases are run for each of the input sets: the bar-magnet-only case, the bar-magnet-and-hysteresis-only case, and the all-torque case. The output based on set 1 is expected; the error follows a downward trend to the right as the integrator order increases and the time step duration decreases. The inclusion of environmental torques results in slightly better performance in most cases. Note that the LGVI output usually exhibits the worst performance at each simulation time step. The LGVI performance is especially poor for the cases which include hysteresis torque; this is likely because the LGVI integrates the hysteresis magnetization using Euler’s method.

The output based on input set 2 is quite different; although the bar-magnet-only case performs better, the cases including dampening torques are much worse as they show little, if any, decrease in beta angle as the integrator order increases and the time step duration decreases. This behavior is believed to be due to the chaotic nature of the separatrix crossing which occurs for case 2 but not for case 1. Figure 8.7 shows the simulation time at which a 1-2-3 Euler Angle error magnitude of one degree is breached using input set 2. At a given time step, each integrator diverges from the “true” attitude at about the same time. This implies that the simulation has entered a chaotic region which causes this divergence. The chaotic behavior does not occur for the bar-magnet-only case (Figure 8.6). This implies that the chaotic region is at some intermediate state such as dampening through the separatrix.

8.3.4 Settling Time Analysis

The presence of a chaotic region does not rule out the possibility of accurate simulation. However, it does mean that the absolute attitude error is perhaps not the best metric for simulation performance. It is possible for the simulated beta angle to accumulate a large phase error without causing a significant change in the settling time. The settling time is chosen as the most important feature of the attitude simulation due to its importance in predicting on-orbit mission duration.

Figure 8.6: The maximum beta angle error for each combination of integrator and time step using input set 1 (top) and input set 2 (bottom) over a 30 hour simulation duration. Each plot shows the performance of the bar-magnet-only case (blue), the bar-magnet-and-hysteresis case (red), and the all-torques case (purple). The beta angle error is defined by comparing the output with the RK7/0.01s output of each case.

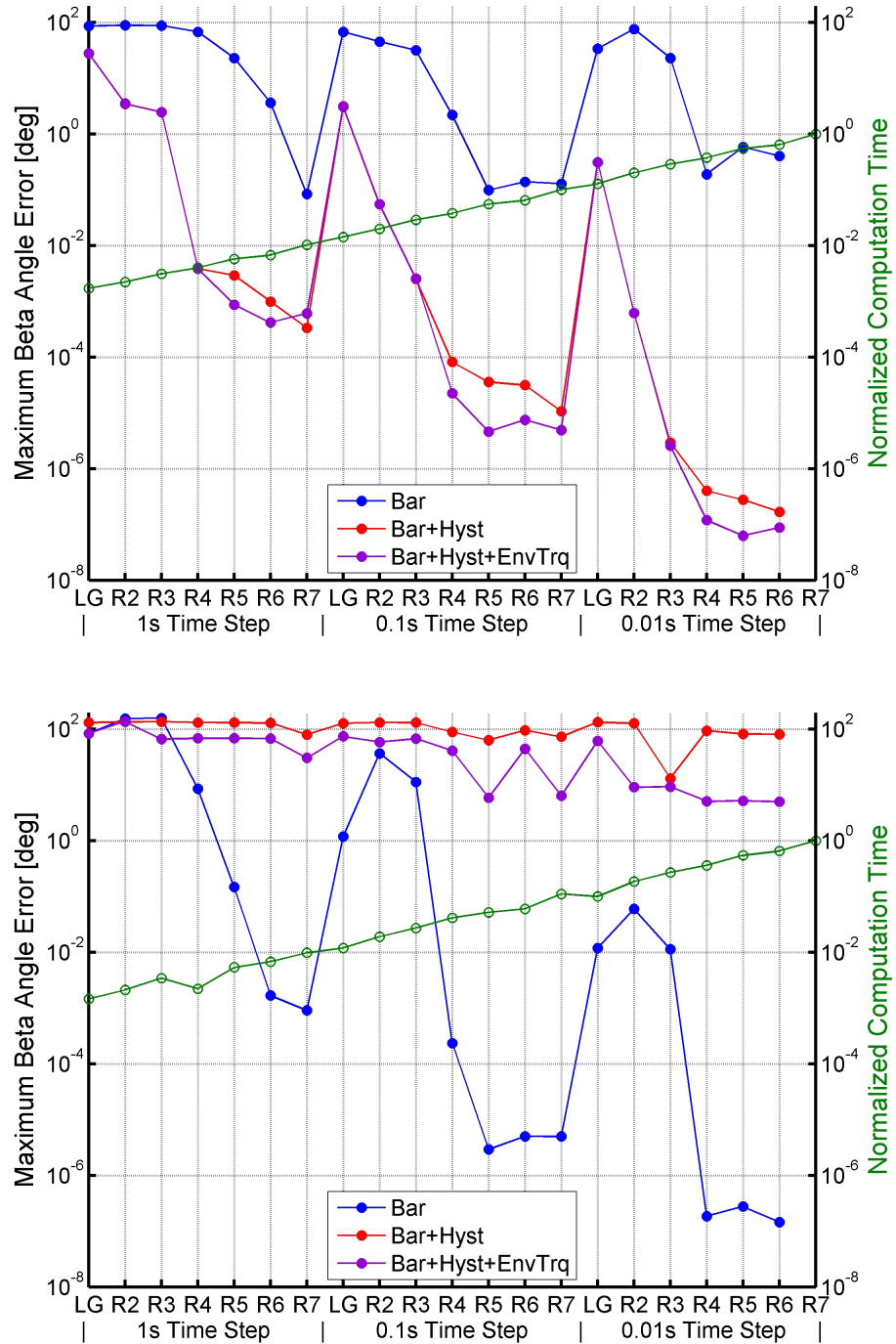
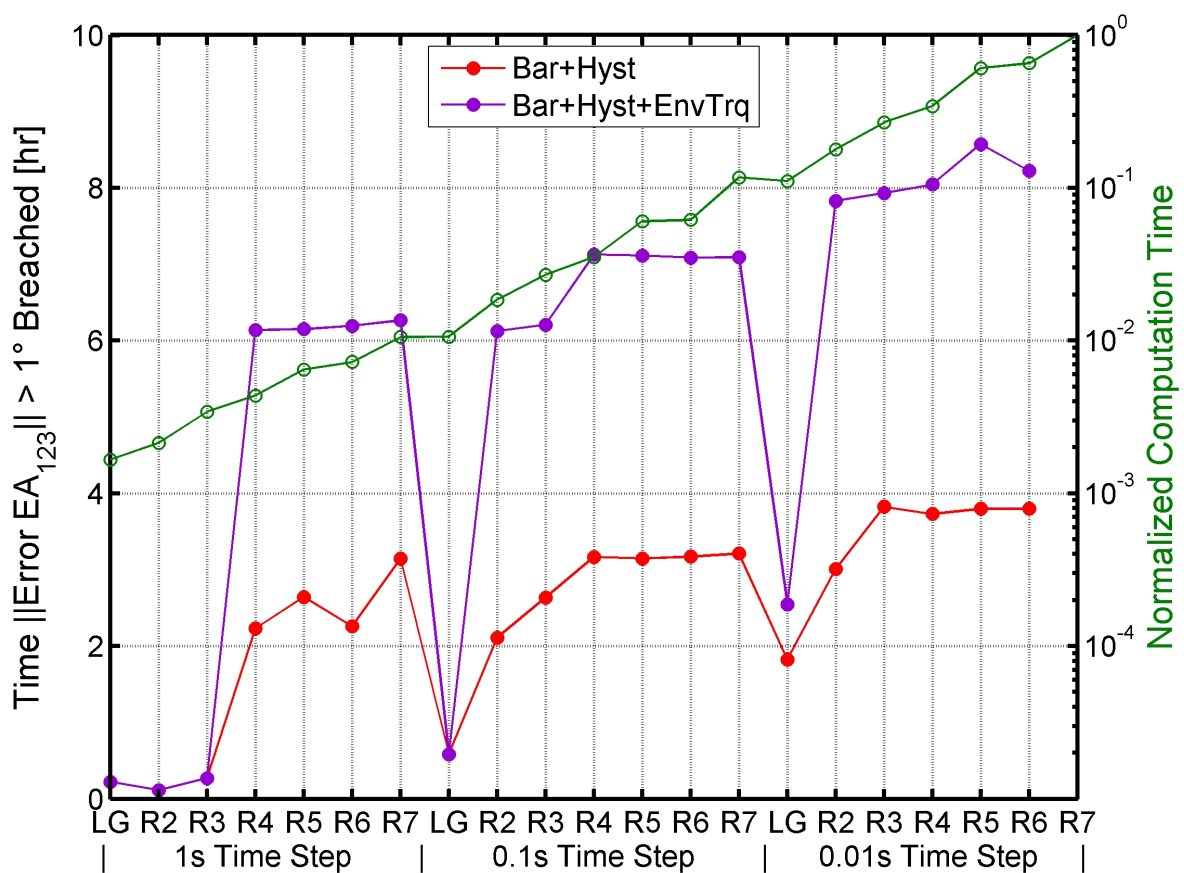


Figure 8.7: The time at which the magnitude of the 1-2-3 Euler angle error exceeds one degree is shown for each integrator and time step combination. These data are generated using initial input set 2.



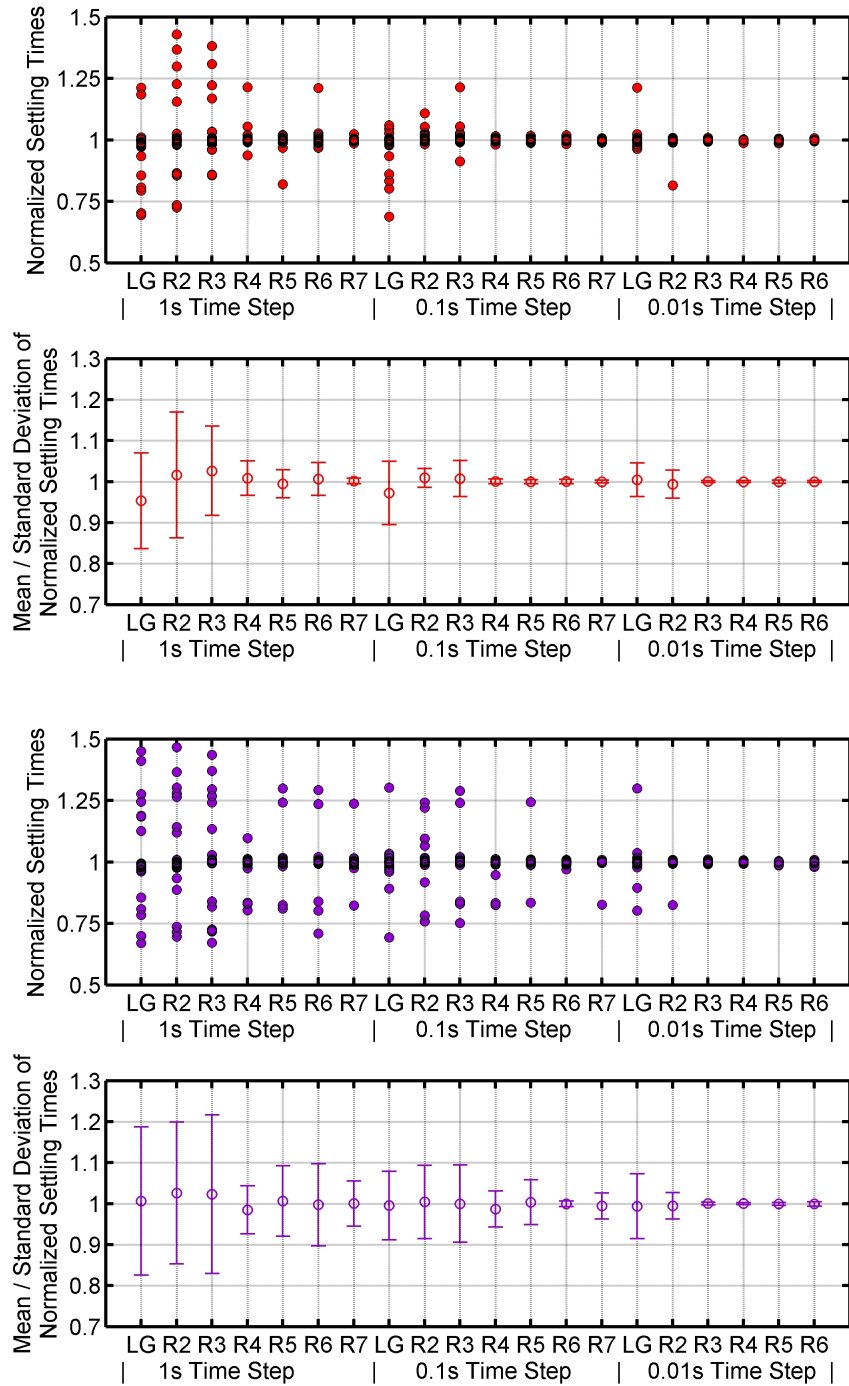
The presence of a chaotic region calls for a different analysis procedure. Initial input set 2 is used as the base input to the simplified simulation. The base input 1-2-3 Euler Angles and angular velocity vector are perturbed by random Gaussian noise. The standard deviation of this noise is set by the 1σ uncertainty of the MEKF fit which defines initial input set 2. The standard deviations are $\sigma_{EA123} = [0.3625 \ 0.6261 \ 0.9539]^T$ in units of degrees and $\sigma_{\omega_0} = [1.4950 \ 2.4140 \ 1.0829]^T \cdot 10^{-2}$ in units of degrees per second. An array of random Gaussian noise values is generated once and loaded before each simulation to ensure that a given run receives identical initial input over the full range of integrator and time step combinations. The simulation is run thirty times and the settling time for each run, integrator, and time step is calculated. Here the settling time is defined as the time after which the beta angle remains within 5° of its final value.

Figure 8.8 shows the settling time distribution, mean, and standard deviation when each run is normalized by its associated RK7/0.01s settling time. The normalized settling times converge as the integrator order increases and the time step duration decreases. This gives confidence that the simplified simulation is converging toward the true settling time for each initial input.

Figure 8.8 is also helpful when deciding upon an integrator and time step for the full simulation. Without non-magnetic torques, RK7 at 1s represents the true system behavior quite well. However, when non-magnetic environmental torques are included in the simulation, RK4 and above at 0.1s or below is necessary to achieve realistic results.

The true settling time is quite sensitive to the initial conditions. Figures 8.9 and 8.10 show initial system energy versus the settling times calculated using RK7/0.01s given normally-perturbed inputs from initial input set 2 for both the bar-magnet-and-hysteresis case and the all-torques case. As shown, the settling time can be quite sensitive to small changes in the initial inputs; the settling times appear to be mostly well-grouped with a few outliers. In order to investigate this behavior further, the sample median for each case is calculated, and bounds are defined for settling times within $\pm 3\%$ of the median; the $\pm 3\%$ threshold is chosen because it is the tightest bound which collects all of the grouped settling times for the bar-magnet-and-hysteresis case. The sample median is used because it is less sensitive to outliers than the sample mean. Pearson's product-moment

Figure 8.8: The simplified simulation normalized settling time, mean, and standard deviation for the bar-magnet-and-hysteresis case (top plots, red) and the all-torques case (bottom plots, purple) using initial input set 2. The settling time for each randomly-perturbed dataset is normalized by the RK7/0.01s settling time of that dataset. The individual settling times for each run are shown on plots 1 and 3 while the mean and standard deviation of the runs for each integrator and time step are shown on plots 2 and 4.



correlation coefficient is calculated for the total and selective samples of each case; the p-value of each correlation coefficient is also determined using a t -distribution with $n - 2$ degrees of freedom, where n is the number of samples in the dataset [80]. The p-value is the probability that the sample correlation could occur by random chance if there is truly no correlation; p-values lower than 0.05 typically represent a statistically significant correlation.

One would expect the initial energy of the system to be strongly correlated with the system settling time. However, the data shows that a significant correlation is only found using settling times within $\pm 3\%$ of the median. All of the calculated settling times appear to represent the true dynamics because the other integrators and time step values converge to the same result, even for the outlying runs (see Figure 8.8). There appears to be some true nonlinear behavior affecting the settling times. However, for all of the RK7/0.01s runs, the settling time does not exceed 110% of the sample median. Rather, the settling time is unexpectedly smaller than it should be. By discretizing the settling times into those above and below 110% of the 30-sample median, a binomial distribution fit finds that the probability of the population of all perturbed simplified simulation runs remaining below 110% has an upper bound of 1 and a lower bound of 0.8843 (with 95% confidence).

This implies that although the PMAC dynamics are very sensitive to initial conditions, the settling time is bounded on the high side. Thus, the nonlinear behavior of the PMAC dynamics is unlikely to cause the settling time to greatly increase. However, the PMAC dynamics may cause the settling time to be significantly smaller than expected. This is good news as it means a simulation can be used to determine the true worst-case settling time of a PMAC satellite.

However, if a simulation is to be used to determine the worst-case settling time, the abnormally low settling times should be avoided. If the simulation is run once and it happens to align with an abnormally-low settling time, a mission designer may incorrectly assume that the expected settling time is lower than it truly is; this incorrect interpretation could impact mission operations. Fortunately, the simplified simulation runs with abnormally low settling times possess a distinct dynamic response. Figures 8.11 and 8.12 show the angular velocity components versus time for

Figure 8.9: The RK7/0.01s settling times versus the initial energy for the simplified simulation perturbation runs of the bar-magnet-and-hysteresis case using the set 2 initial inputs. The left plot shows the settling times for all thirty cases run and uses the dotted black lines to bound values within 3% of the sample median shown by a solid red line; values outside these bounds are represented by empty circles while values within the bounds are represented by filled red circles. The right plot shows only those settling times within 3% of the entire dataset median. Pearson's product-moment correlation coefficient and the associated p-value are shown for the data within each plot.

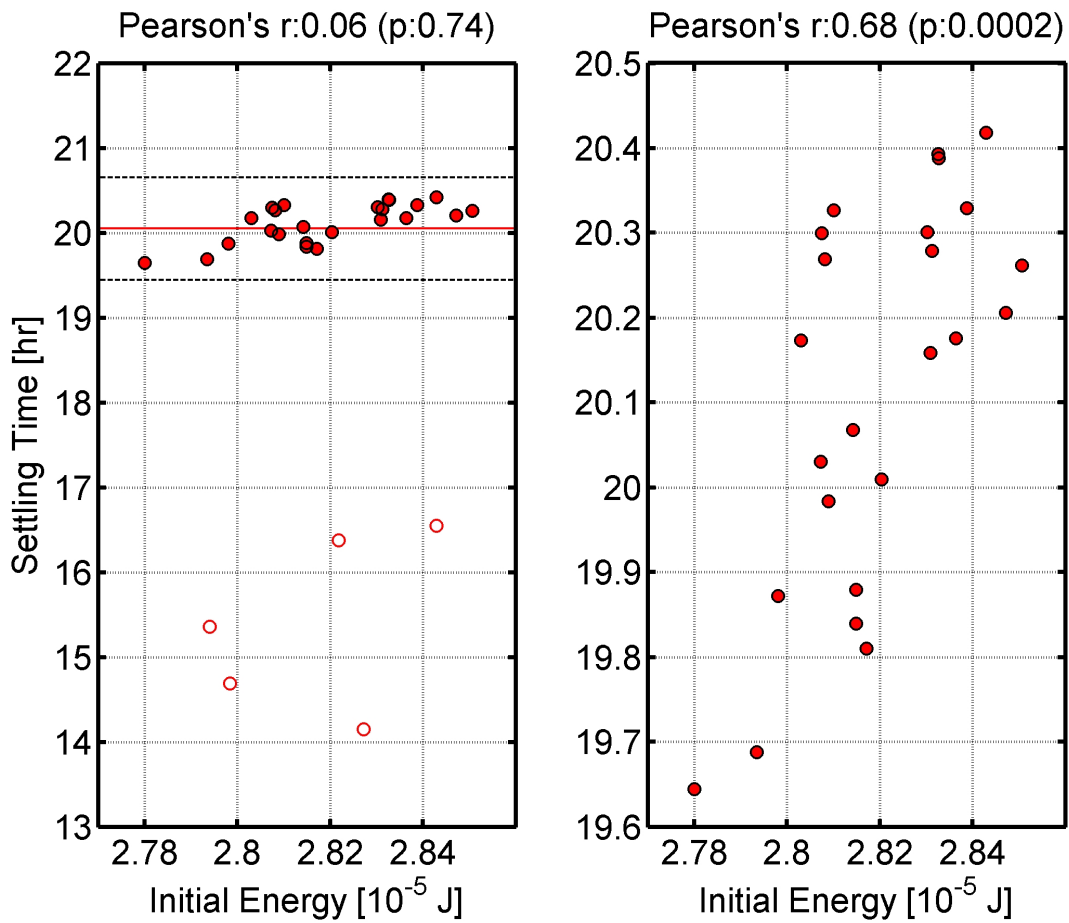
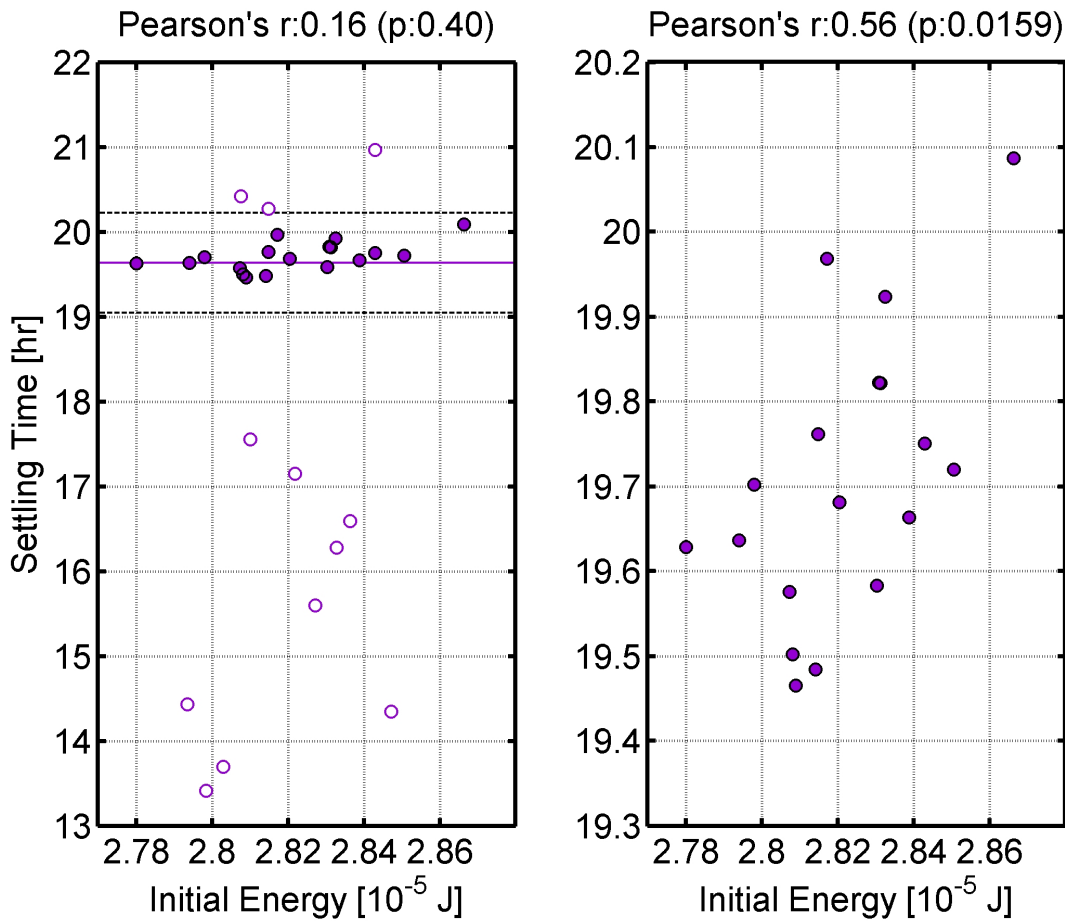


Figure 8.10: The RK7/0.01s settling times versus the initial energy for the simplified simulation perturbation runs of the all-torques case using the set 2 initial inputs. The left plot shows the settling times for all thirty cases run and uses the dotted black lines to bound values within 3% of the sample median shown by a solid purple line; values outside these bounds are represented by empty circles while values within the bounds are represented by filled purple circles. The right plot shows only those settling times within 3% of the entire dataset median. Pearson's product-moment correlation coefficient and the associated p-value are shown for the data within each plot.



each of the 30 perturbed initial input set 2 simulations for the bar-magnet-and-hysteresis and the all-torques cases; the runs which have a settling time below 95% of the sample median are shaded.

The figures show that the normal response of the satellite is to achieve a mostly flat spin about the major inertia axis ${}^B X$ early in the simulation. The satellite remains in this configuration until ω_X has damped to the level of ω_Y . At this point, the rotation is transferred solely to ${}^B X$ and ${}^B Z$ in the form of roll- and yaw-wobble about the constant magnetizing field. Note that the sign of the major inertia axis rotation ω_X flips at random; this is anticipated when traveling through the chaotic separatrix. The angular velocity response of each simulation with low settling time is quite different and easy to distinguish from the normal case. Thus, the angular velocity response of the simplified simulation output can give clues to its reliability. The response of the full simulation may be equally helpful in determining its validity.

8.3.5 Summary

An analysis of the energy conservation of each integrator showed that, for PMAC simulation, higher order Runge-Kutta methods are comparable to LGVI in both energy conservation and computation time. Energy conservation analysis shows that acceptable numeric integrator performance is dependent on the time step. Generally, RK4 and above at a time step of 0.1s or smaller yields acceptable energy conservation at the worst-case initial input considered.

Beta angle analysis shows that Runge-Kutta methods clearly outperform LGVI in limiting absolute attitude error. However, this analysis also shows that the absolute attitude error is difficult to minimize for a PMAC simulation with hysteresis in certain initial conditions. This is likely due to the satellite traveling through the chaotic separatrix with continued energy dissipation.

The settling time analysis shows that all integrators and time steps converge to one settling time for each run of identical perturbed initial conditions. This behavior is interpreted as the simulation converging to the true dynamics of the system. However, the true settling time is very sensitive to the initial conditions. The perturbation analysis shows that small changes in the initial state can lead to abnormally low settling times. For the simplified simulation, this abnormal

Figure 8.11: The RK7/0.01s angular velocity components versus time for each of the simplified simulation runs of the bar-magnet-and-hysteresis case using initial input perturbed from input set 2. The axis labels have been omitted from each plot for clarity. For each plot, the vertical axis ranges from -4 to 4 degrees per second while the horizontal axis ranges from 0 to 30 hours. The angular velocity components ω_X , ω_Y , and ω_Z are shown in blue, green, and red, respectively. The runs which result in a settling time less than 95% of the sample median are shaded.

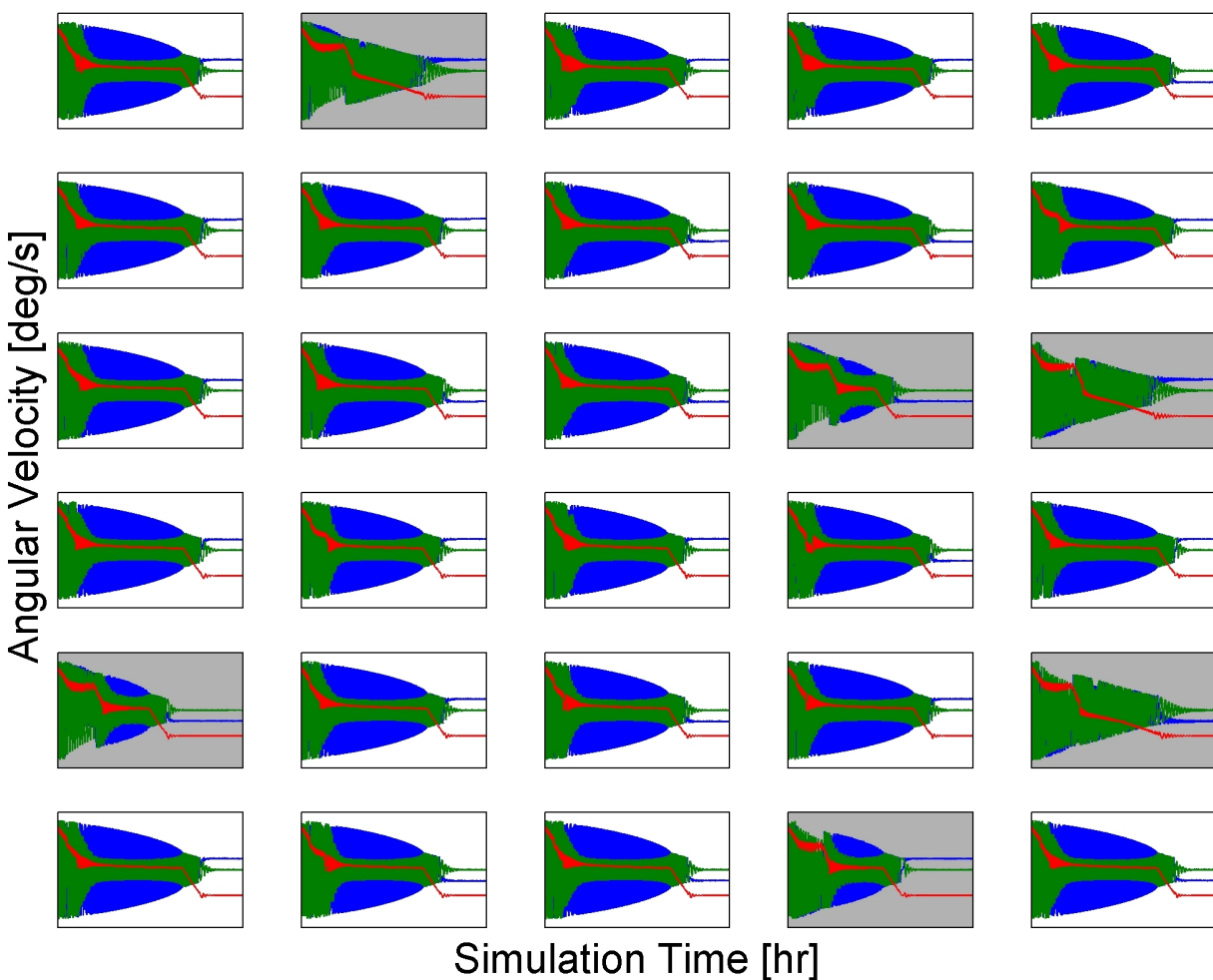
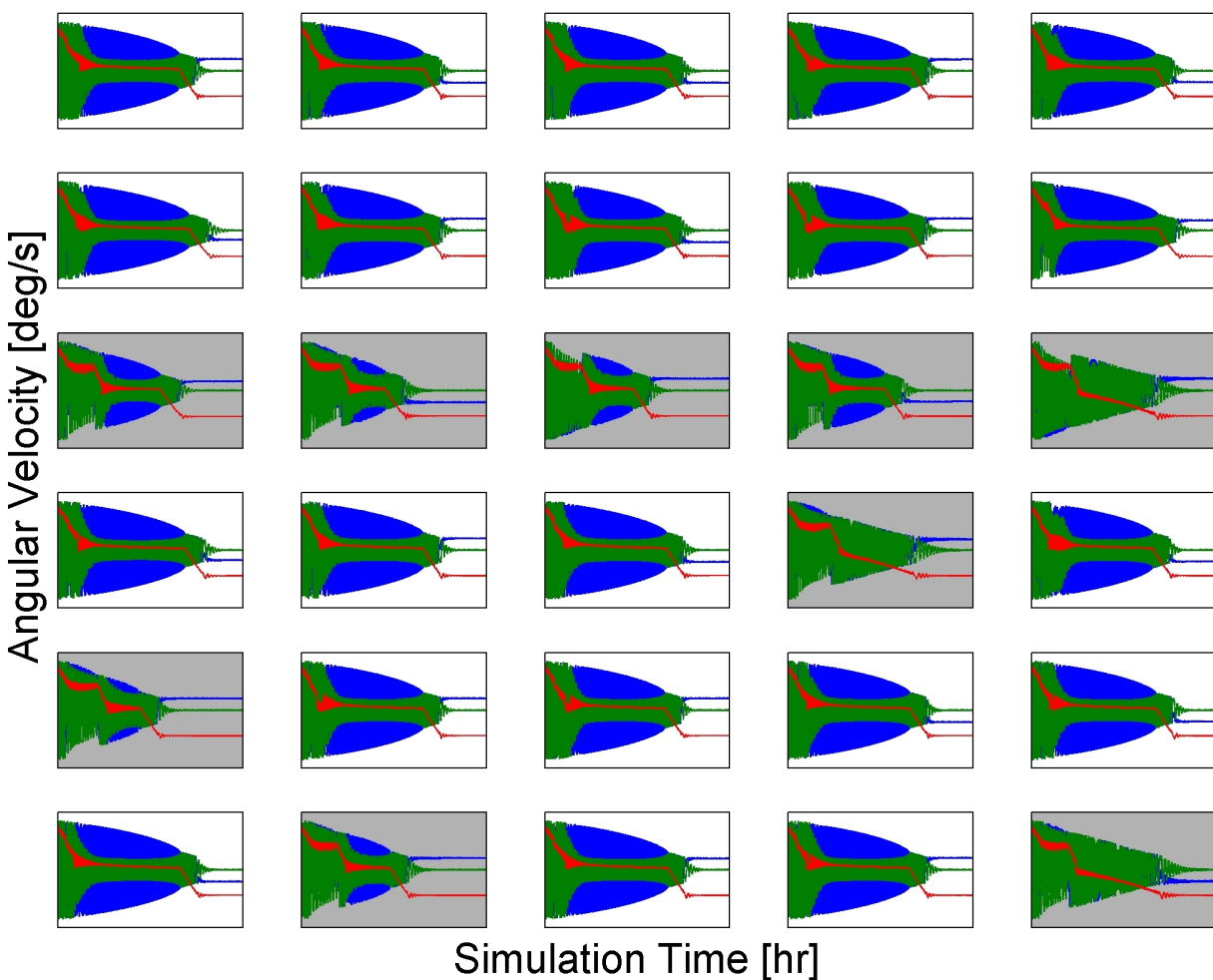


Figure 8.12: The RK7/0.01s angular velocity components versus time for each of the simplified simulation runs of the all-torques case using initial input perturbed from input set 2. The axis labels have been omitted from each plot for clarity. For each plot, the vertical axis ranges from -4 to 4 degrees per second while the horizontal axis ranges from 0 to 30 hours. The angular velocity components ω_X , ω_Y , and ω_Z are shown in blue, green, and red, respectively. The runs which result in a settling time less than 95% of the sample median are shaded.



behavior can be identified by the dynamic response of the simulation over time.

8.4 Results

Before the results are presented, the nominal simulation inputs are defined. Nominal case outputs such as beta angle, angular velocity, and system energy are presented. This nominal output is compared to on-orbit data and the magnetic-torque-only case.

8.4.1 Nominal Input

The full PMAC simulation nominal inputs are shown in Table 8.2. The RK4 integrator at 0.1s time step is chosen as the nominal case; simplified simulation showed this combination to have low rates of settling time error (see Figure 8.8) at moderate computational cost. Also, RK4 leaves higher orders of Runge-Kutta at the same time step for output comparison.

The hysteresis rod loop parameters are set by the best fit to the measured hysteresis rods (see Section 7.3.4.3). The moments of inertia are based on the SolidWorks model of the CSSWE spacecraft. The distance vector from the satellite CG to the geometric center r_d is also given by the SolidWorks model. The ap index and F10.7 flux values are given by data from the previous solar cycle; the selected values overestimate the true solar activity which was actually experienced over the first ten days on orbit (the true 10-day average values of ap index and F10.7 flux were 6.1 and $113.7 \cdot 10^{-22} \text{ W} \cdot \text{m}^{-2} \text{Hz}^{-1}$, respectively [2]). The early-mission CSSWE TLE is used as input to the SGP4 orbit propagator.

The base initial angular velocity vector and initial 1-2-3 Euler angles are equivalent to the simplified simulation initial input set 2, which is defined by early-mission CSSWE MEKF output. As with the analysis presented in Section 8.3.4, the initial attitude and angular velocity vector are perturbed by normal Gaussian noise with a standard deviation equivalent to the 1σ uncertainty of the MEKF filter output. This process allows the simulation performance to be examined over a number of perturbed initial inputs. However, the data from a single initial input set is used as the nominal output and presented below.

Table 8.2: Nominal inputs for the full simulation are shown below. Most inputs are based on CSSWE values; all inputs are given in the body frame when applicable.

Parameter	Value	Unit
Numeric Integrator	RK4	
Time step duration h	0.1	s
Simulation Start Date/Time	2012.09.14 00:59:48	UTC
Base Initial 1-2-3 Euler Angle EA_{123}	[13.9 -71.6 104.1]	deg
Base Initial angular velocity vector ω_0	[0.17 -0.97 2.93] ^T	deg/s
Initial magnetic field offset β	178.1	deg
X-axis moment of inertia I_{xx}	$2.22 \cdot 10^{-2}$	kg·m ²
Y-axis moment of inertia I_{yy}	$2.18 \cdot 10^{-2}$	kg·m ²
Z-axis moment of inertia I_{zz}	$5.00 \cdot 10^{-3}$	kg·m ²
Bar magnet magnetic moment vector \mathbf{m}_{bar}	[0 0 0.55] ^T	A·m ²
Number of hysteresis rods per body axis	[3 3 0] ^T	
Hysteresis rod length	95	mm
Hysteresis rod diameter	1	mm
Initial hysteresis rod magnetic flux density	0	Tesla
Hysteresis rod coercivity H_c	0.3381	A/m
Hysteresis rod remanence B_r	$6.0618 \cdot 10^{-4}$	Tesla
Hysteresis rod saturation B_s	0.3000	Tesla
Residual magnetic moment vector ${}^B\mathbf{m}_{\text{res}}$	[0.0059 0.0083 -0.0004] ^T	A·m ²
Satellite coefficient of drag C_d	2.4	
Distance vector from satellite CG to geometric center \mathbf{r}_d	[2.601 -0.218 -8.086] ^T	mm
Satellite surface area by body axis S	[0.01 0.03 0.03] ^T	m ²
Satellite coefficient of reflectivity c_R	0.8	
3-hour ap index average for the last 57 hours	48	
81-day average F10.7 flux	$168.5 \cdot 10^{-22}$	W·m ⁻² Hz ⁻¹
Daily F10.7 flux for previous day	$128.7 \cdot 10^{-22}$	W·m ⁻² Hz ⁻¹
Solar pressure at earth P_S	$4.5 \cdot 10^{-6}$	N·m ⁻²
TLE		
1 90039U 0	12268.58971383	+ .00002482 +00000-0 +23852-3 0 00208
2 90039 064.6731 007.9077 0219372 286.2692 203.1718 14.79135411001569		

8.4.2 Nominal Output

The nominal simulation output is shown using a variety of plots. Figure 8.13 shows the components of angular velocity simulating the first ten days after orbit insertion. Angular velocity is exchanged between satellite axes in accordance with the difference in mass moment of inertia of the axis (as expected from Equation 2.3). The roll rate is observed to rapidly oscillate in the early motion as the satellite is in a full tumble; no single axis dominates the angular velocity vector. The tumble becomes more controlled approximately 2.5 days after orbit insertion when the motion is mainly about the major inertia axis. However, the major inertia spin dampens to the level of intermediate axis while the roll rate steadily climbs. The final settling to a non-zero roll rate is intuitive; a PMAC satellite cannot rotate about any other axis while the bar magnet remains parallel to the magnetic field.

Figure 8.14 shows the kinetic, potential, and total rotational energy of the simulated satellite. A nearly linear decrease in energy is visible over the first four days. Immediately following day six, the satellite kinetic energy remains at a constant nonzero value. Post-settling variations in the potential energy are due to magnetic field amplitude changes throughout the satellite orbit.

Figure 8.15 shows the β angle between the BZ -axis and the local magnetic field vector. A green line has been added to represent settling at $\beta \leq 10^\circ$. Although the instantaneous beta changes rapidly, the maximum beta angle decreases nearly linearly over time, reflecting the system energy behavior. The simulation finds that the satellite settles to the magnetic field six days after PPOD deployment. Following settling, the beta angle remains within five degrees of the local magnetic field.

The next plots show the simulation output before and after settling occurs using 100-minute (about one orbit) datasets. The pre- and post-settling datasets are the simulation output at orbit 15 and 105, approximately 1 and 7 days after PPOD deployment. Figure 8.16 shows the relative magnitudes of the external torques acting on the satellite over both orbits.

The bar magnet dominates the other torques in the early mission; post-settling it is at the level

Figure 8.13: The nominal simulation output body-frame angular velocity vector components are shown. Yaw (blue) is about the ${}^B X$ (maximum inertia) axis, pitch (green) is about the ${}^B Y$ (intermediate inertia) axis, and roll (red) is about the ${}^B Z$ (minor inertia) axis.

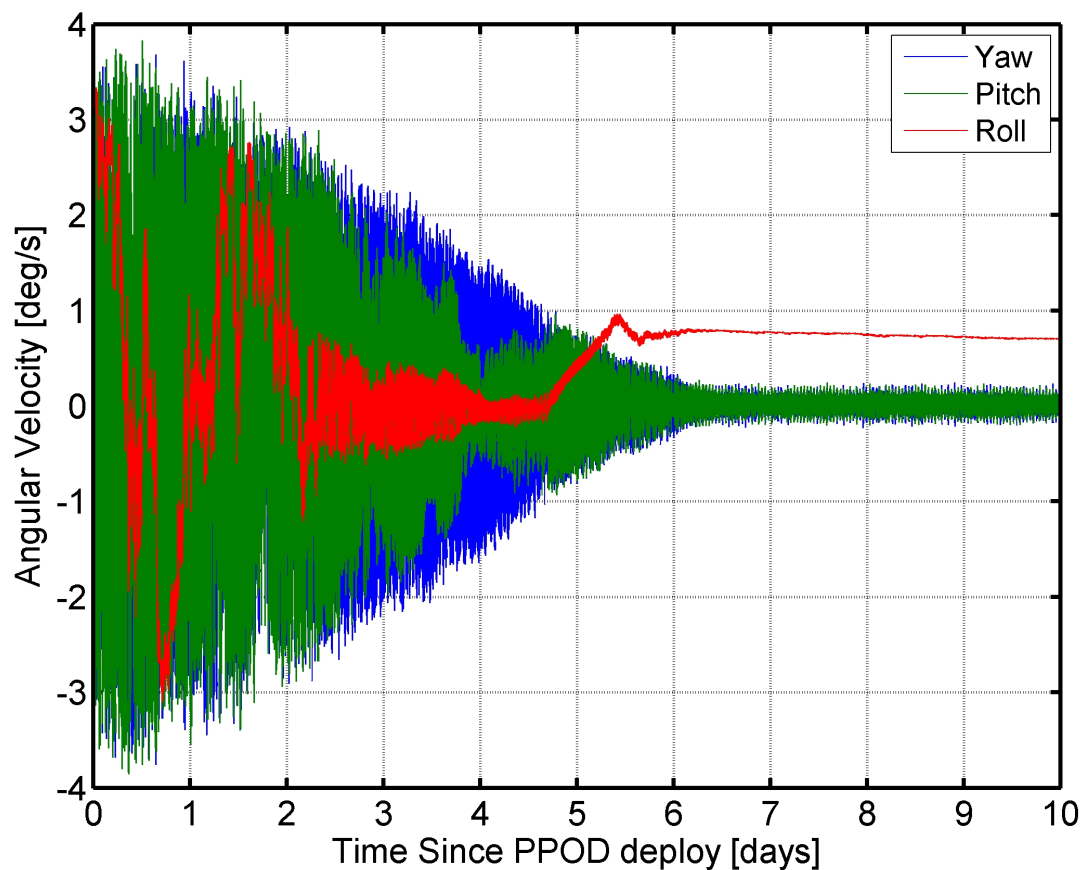


Figure 8.14: The kinetic, potential, and total satellite rotational energy values are shown. The total energy settles to a constant offset from the potential energy due to a non-zero kinetic energy.

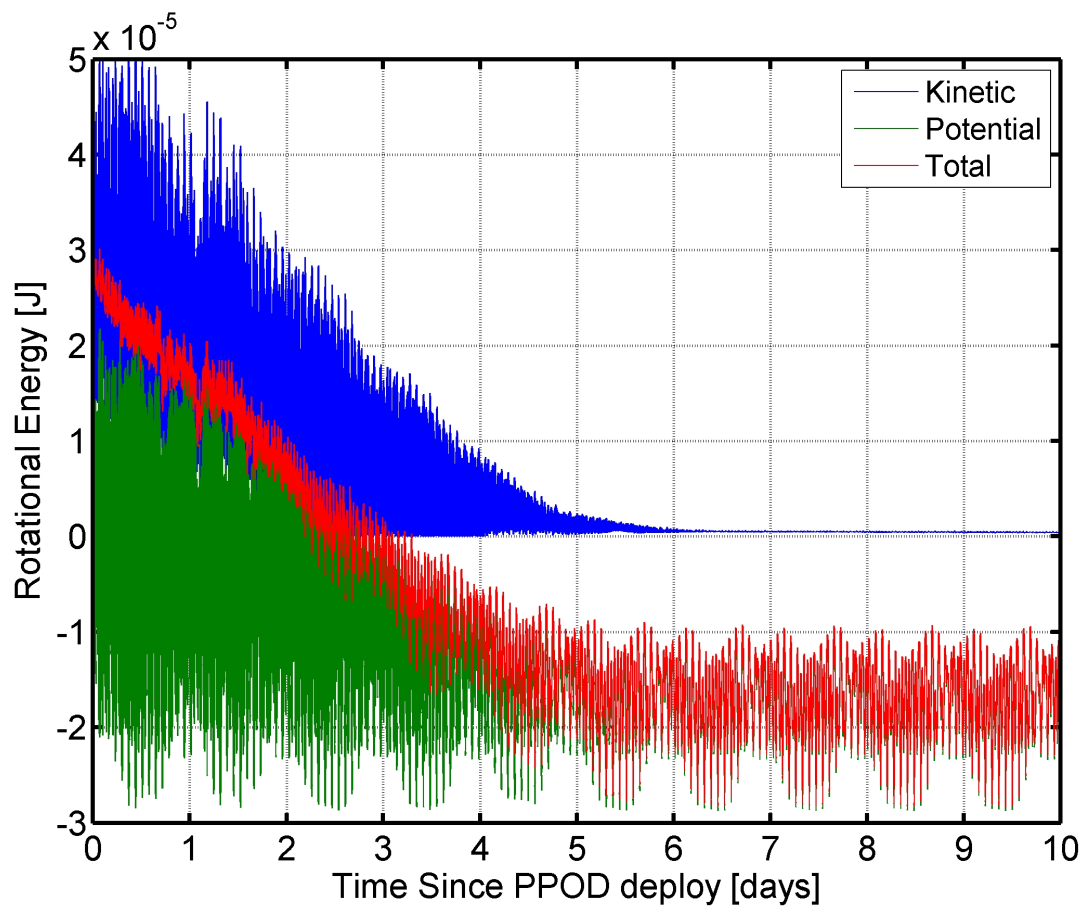
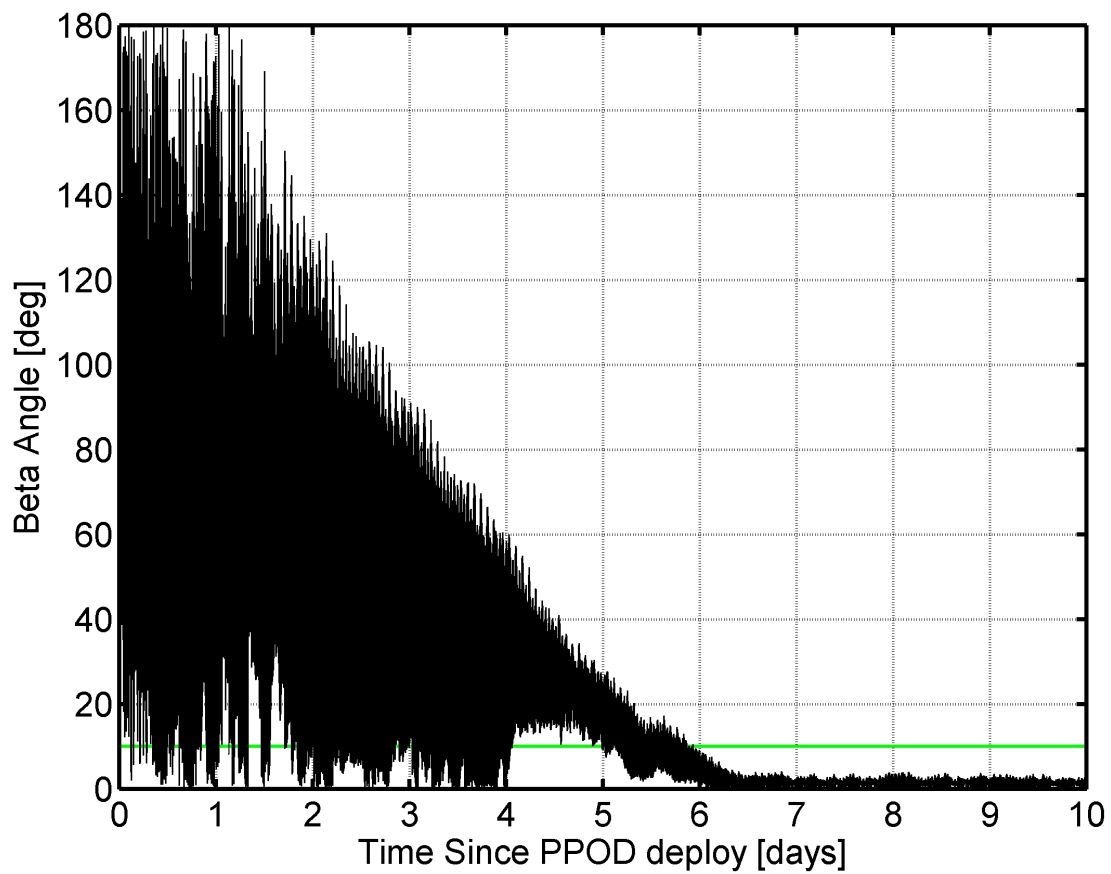


Figure 8.15: The β angle between BZ -axis and the local magnetic field vector is shown. A green line has been added at the value $\beta = 10^\circ$; this is used as the attitude settling threshold.



of the magnetic residual torque and the gyroscopic torque. Even before settling, the gyroscopic torque is within an order of magnitude of the bar magnet torque and at times is the dominant torque. This means that torque-free motion must be considered as it likely has a substantial effect on the system dynamics. The hysteresis rods lose an order of magnitude of torque from pre- to post-settling; they are demagnetized by decreasing H-field amplitude cycles as the satellite aligns. In the early mission, the hysteresis rods dominate the time-varying external torques but by late mission, the hysteresis torque is at the level of the gravity gradient and drag torques. After settling, the energy dissipation provided by hysteresis is in equilibrium with the energy input from the non-magnetic environmental torques. As expected, the eddy current torque is higher during the early mission which has higher rotation rates.

Figure 8.17 shows the hysteresis loops traced during the early- and late-mission orbits. The rods experience a much larger range of magnetizing fields before settling occurs. The hysteresis bounds remain the same throughout the simulation as they are directly set by the hysteresis parameters (H_c , B_r , and B_s) which do not change. The loops are thin and hard to distinguish in the early mission. After settling, the magnetization output is observed to produce small loops, always within the bounds of the inverse tangent loop. These “minor loops” are expected for ferromagnetic materials experiencing a magnetizing field insufficient to reach saturation [17]; the simulation is correctly modeling the low cycle amplitude hysteresis response. As mentioned previously, the traced hysteresis loop area is equivalent to the energy dissipated from the system. After settling, the hysteresis dampening is in equilibrium with the energy input by non-magnetic external torques; the constant magnetic external torques \mathbf{L}_B and \mathbf{L}_R cannot add or remove energy from the system.

Figure 8.17 shows a troubling characteristic of the Flatley model using the fitted hysteresis parameters. In the early mission orbit, an average of 34% of the hysteresis magnetizations need correction after each simulation time step. The late mission orbit does not require any corrections. It is difficult to determine the effect of the correction frequency; removing the correction in the early mission causes the simulated magnetization to exceed the inverse tangent bounds and become unrealistic. This is a drawback of the Flatley model, but the effect does decrease slightly for higher-

Figure 8.16: The magnitude of each external torque acting on the spacecraft is shown for the pre-settling orbit 15 (top) and the post-settling orbit 105 (bottom). Note the change of scale for the y-axis between the two plots. Here \mathbf{L}_{GY} is the gyroscopic motion torque ($[\omega \times] [I] \omega$), \mathbf{L}_B is the bar magnet torque, \mathbf{L}_H is the hysteresis torque, \mathbf{L}_{GG} is the gravity gradient torque, \mathbf{L}_D is the drag torque, \mathbf{L}_{SP} is the torque due to solar pressure, \mathbf{L}_R is the magnetic residual torque, and \mathbf{L}_{EC} is the eddy current torque.

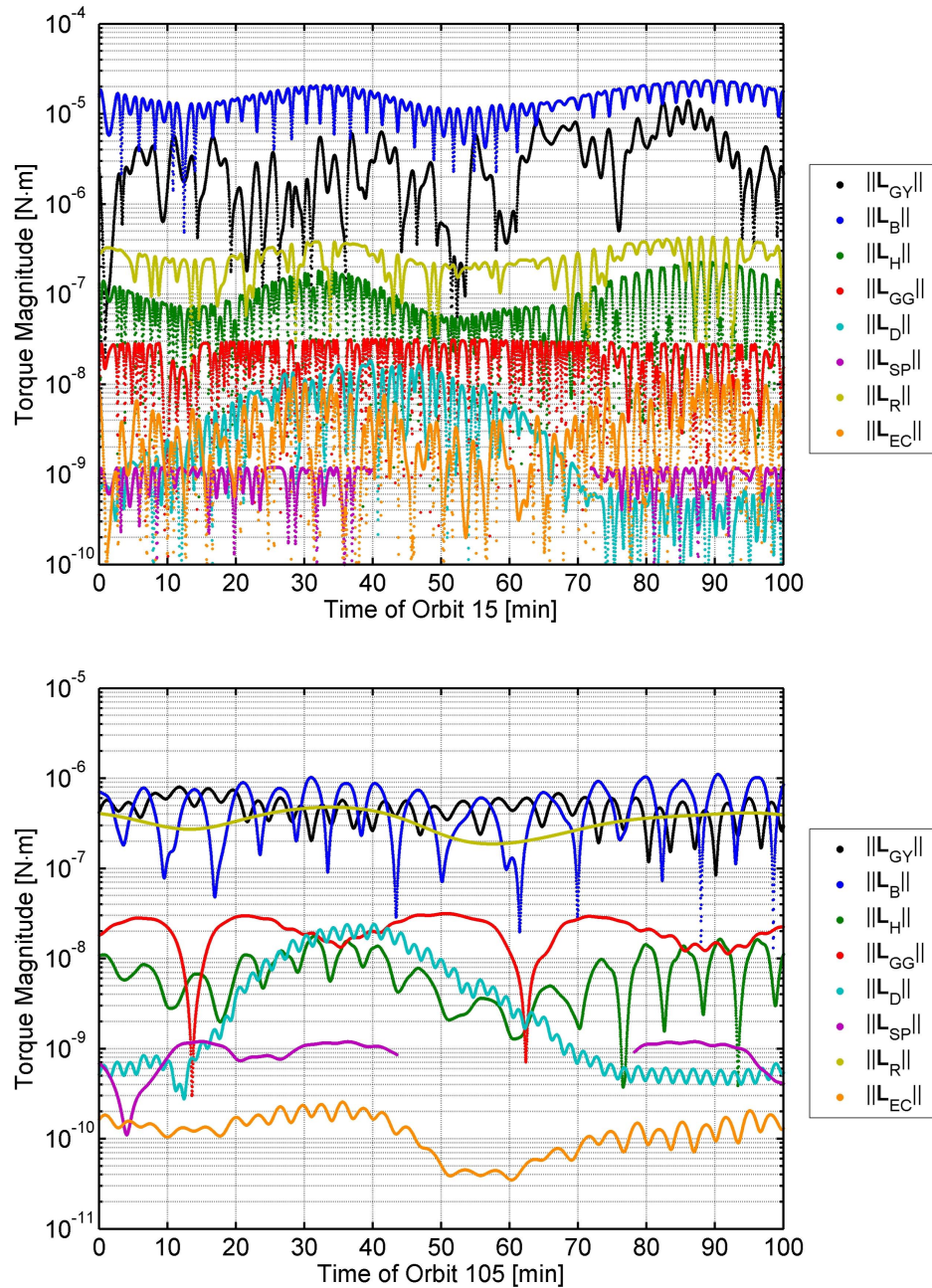
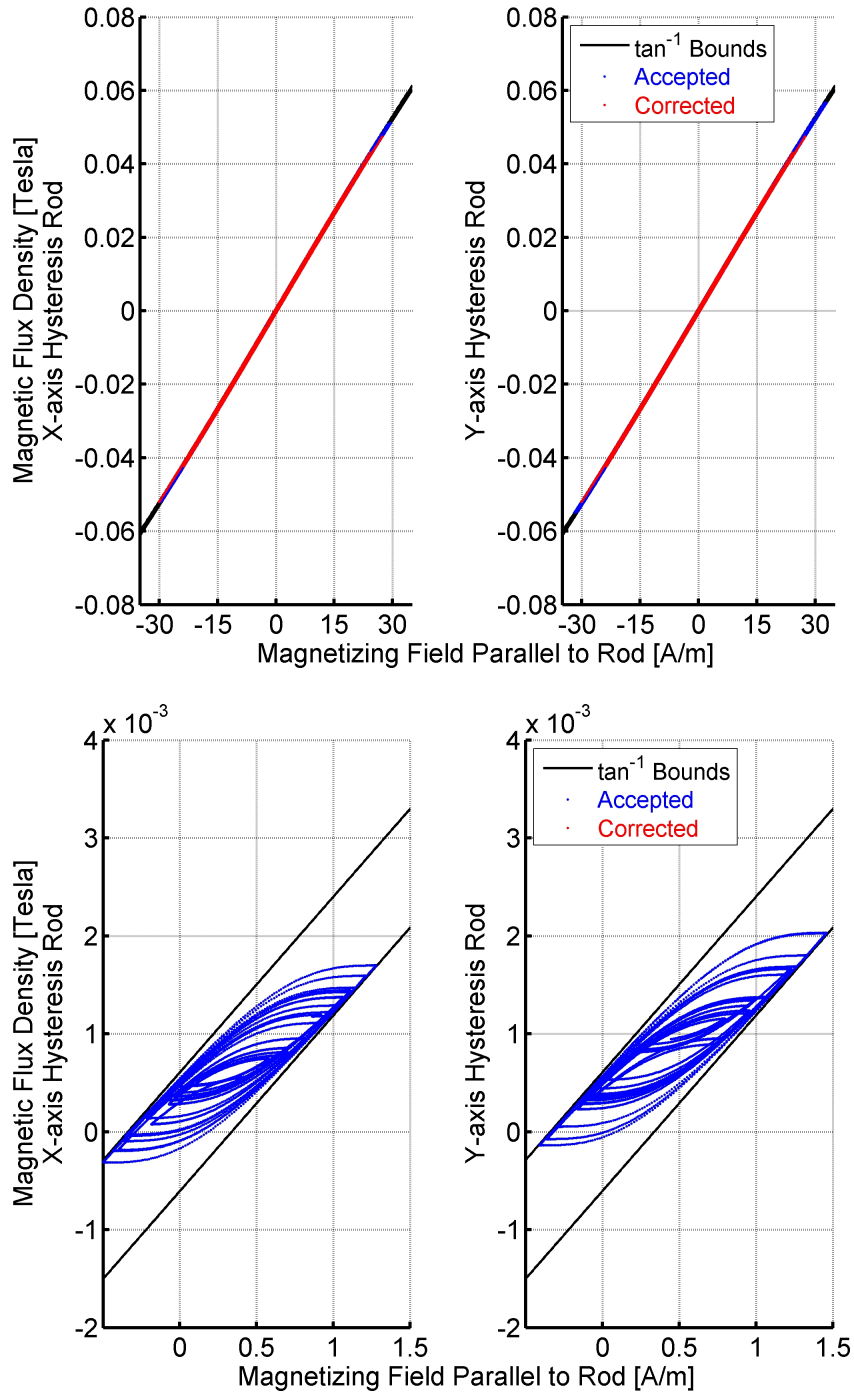


Figure 8.17: The single-orbit X- and Y-axis hysteresis loops simulated before (top) and after (bottom) the attitude settles. The inverse tangent bounds of the Flatley hysteresis model are shown. The magnetizations which have been corrected to remain within the inverse tangent bounds are shown in red; all other output is shown in blue.



order integrators at low simulation time step values.

8.4.3 High-Order Integrator Comparison

Although the simplified simulation showed the adequate performance of the RK4 at a 0.1s time step, confidence can be gained by comparison with a higher-order integrator such as the RK7 at the same time step. This section collects the results of this comparison analysis. Figure 8.18 compares the angular velocity components of both integrators. Both integrators display early-simulation rapid roll rate variation, mid-settling near-zero roll rate, and post-settling constant roll rate. The amplitude of the roll rate is inverted for the RK7 case; this may be due to chaotic dynamics during settling. Both datasets show most flat spin about the major inertia axis in the middle of attitude settling.

Figure 8.19 compares the energy response of the RK4 and RK7 integrators. The responses are quite similar, although the RK7 dampens the kinetic energy significantly quicker than the RK4 integrator. Note that the RK7 does not experience the jump in kinetic energy one day after PPOD deployment. This may represent a sensitive dynamics region which happened to increase the energy for RK4 but not for RK7, causing the RK4 simulation to have a longer settling time.

Figure 8.20 compares the beta angle as generated by the two integrators. The decreased energy of the RK7 simulation causes the attitude to settle in five days instead of six. The structure of the beta angle is similar for both cases; both show a linear decrease in the maximum beta angle over time. Both begin to track the magnetic field at an offset before slowly removing the offset over the course of about 36 hours. Further simulations are necessary to determine the cause of the difference in settling times.

8.4.4 On-Orbit Data Comparison

The output from the simulation may be verified by comparison with data filtered from the on-orbit attitude measurements of the CSSWE satellite. The initial conditions of the simulation are set based on the filtered data of the satellite close to its deployment from the PPOD. If the

Figure 8.18: Angular velocity components of the RK4 and RK7 integrators are shown. Yaw (blue) is about the ${}^B X$ (maximum inertia) axis, pitch (green) is about the ${}^B Y$ (intermediate inertia) axis, and roll (red) is about the ${}^B Z$ (minor inertia) axis.

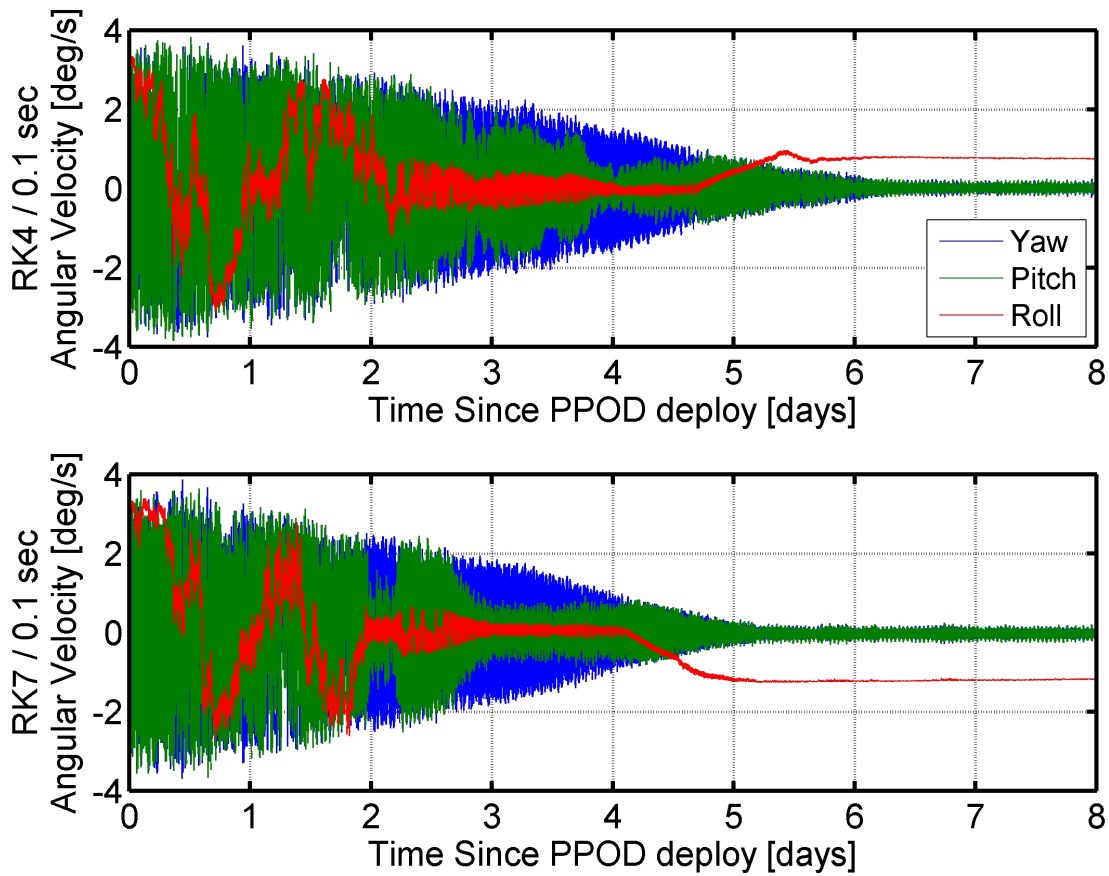


Figure 8.19: The kinetic (blue), potential (green), and total (red) rotational energy as calculated by the RK4 (top) and RK7 (bottom) integrators.

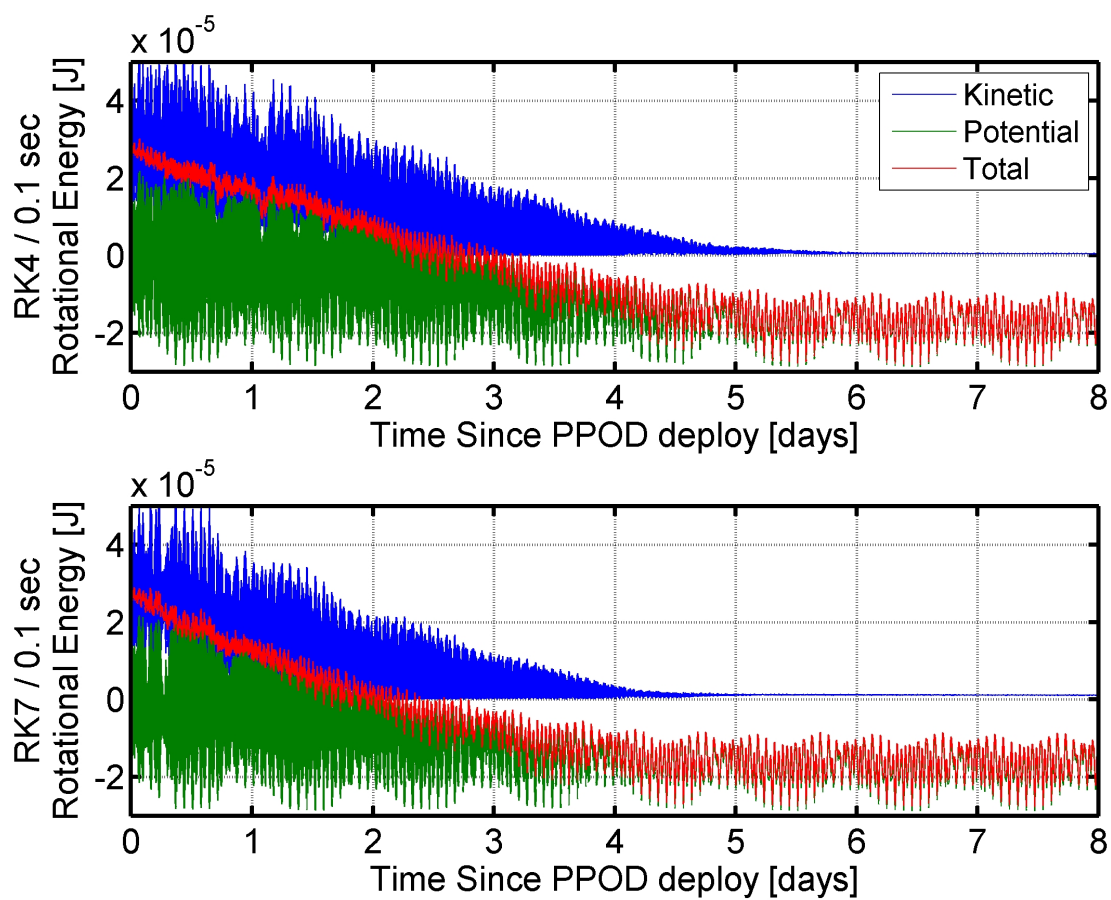
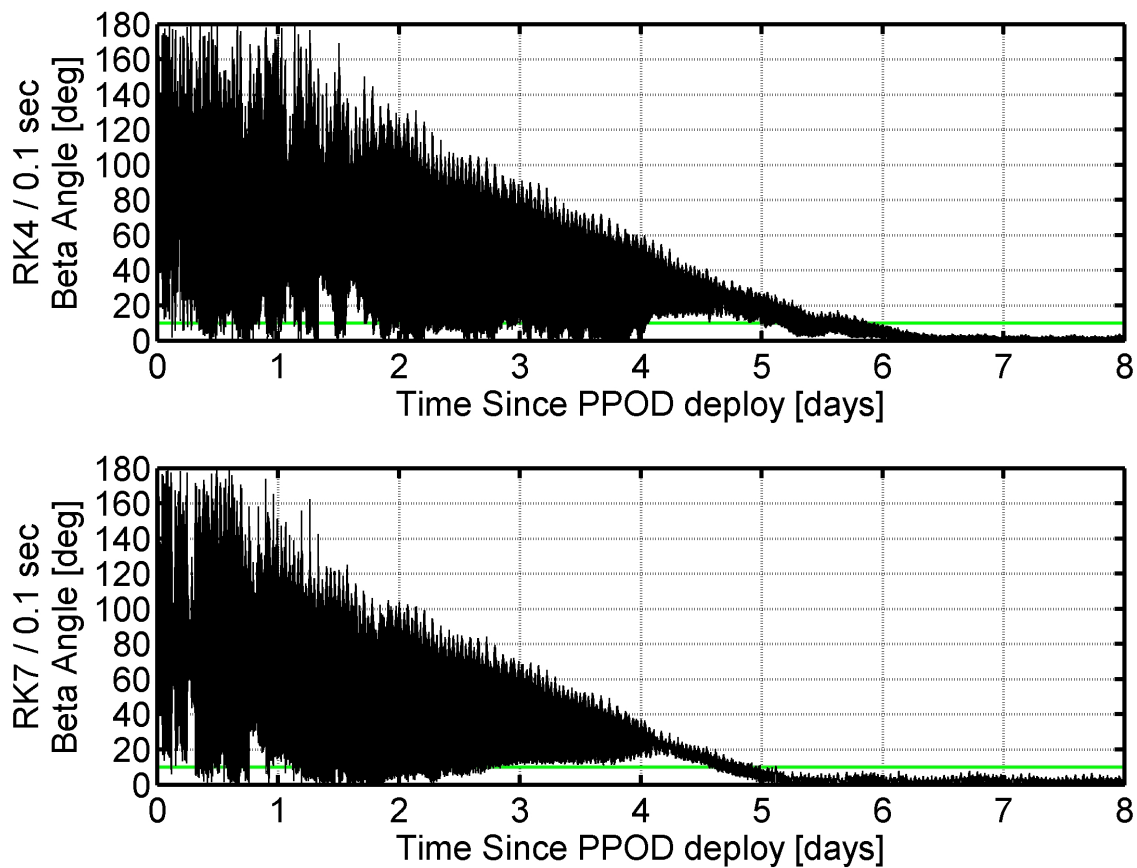


Figure 8.20: The β angle between the local magnetic field and the BZ axis as calculated by the RK4 (top) and RK7 (bottom) integrators is shown. A green line at $\beta = 10^\circ$ has been added to show the settling threshold.



simulation is valid, it should roughly agree with the MEKF output.

The angular velocity is compared in Figure 8.21; similar behavior is observed. The roll rate shows equivalent variation in the first few days after deployment. The filtered data shows that the satellite maintains a near-zero roll rate for a short duration 2.5 days after PPOD deployment before approaching a roll rate of $-1^\circ/\text{s}$ until day six. The simulated data remains at a near-zero roll rate longer before settling to $1^\circ/\text{s}$ shortly before settling. The CSSWE attitude response does not experience a flat spin about any axis before settling. Instead, the angular velocity is equally shared between the intermediate- and major-inertia axes over the entire timespan.

Figure 8.22 compares the simulated and measured system rotational energy. The simulation does not model the antenna deployment event which occurs two hours after deployment and changes the bar magnet moment from $0.84 \text{ A}\cdot\text{m}^2$ to $0.55 \text{ A}\cdot\text{m}^2$ (see Section 6.3.2.1). This event causes the discontinuity seen in the filtered energy shortly after deployment. However, after the event, the total energy is roughly equal to the simulated condition. The simulated energy loss is more linear than the experimental data shows. This is likely because the Flatley hysteresis model accuracy degrades as the simulated magnetizing field cycle amplitude diverges from the experimental cycle amplitude used to generate the hysteresis fit parameters (see Section 7.3.4.1).

Because of the limitations of the model, the parameters were fitted to experimental data collected at $\pm 10 \text{ A/m}$ and $\pm 20 \text{ A/m}$. At cycle amplitudes larger than the fitted experimental datasets (such as shortly after PPOD deploy), the Flatley model will underestimate the hysteresis dampening. However, if the simulated cycle amplitude is much less than the fitted experimental datasets, the Flatley model may cease representing hysteresis as a closed loop (as shown Figures 7.15 and 7.16). The net effect of these errors is to linearize the simulated hysteresis dampening. The experimental data also shows that the energy dissipation continues after settling, when the majority of the rotation is about the roll axis; this simulation does not show this behavior.

Figure 8.23 compares the simulated and filtered β angle. CSSWE settles to the local magnetic field 6.5 to 7.5 days after PPOD deploy; this is comparable to the simulated six day settling time. The beta angle structure reflects the differences in energy dissipation shown previously; the

Figure 8.21: The angular velocity vector components as simulated by the RK4 at 0.1s (top) and as measured by the MEKF output of CSSWE data (bottom). Yaw (blue) is about the ${}^B X$ (maximum inertia) axis, pitch (green) is about the ${}^B Y$ (intermediate inertia) axis, and roll (red) is about the ${}^B Z$ (minor inertia) axis.

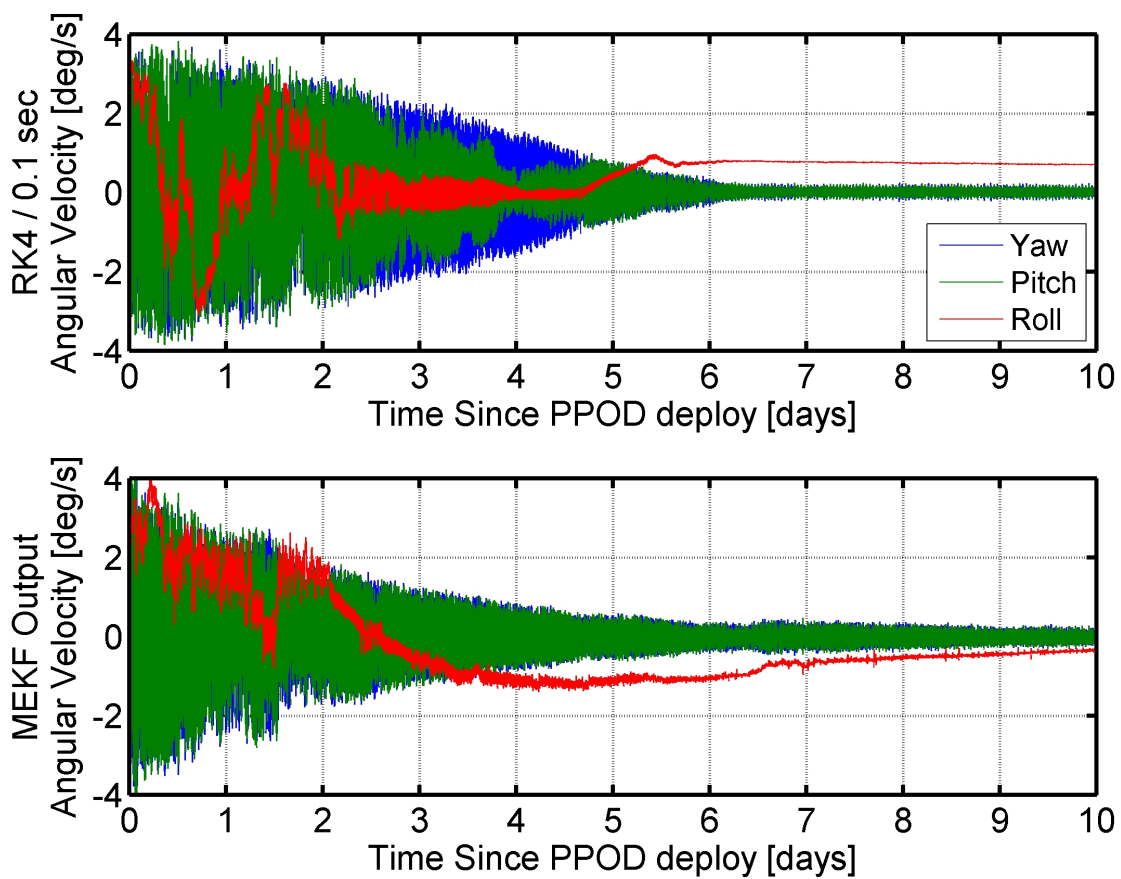
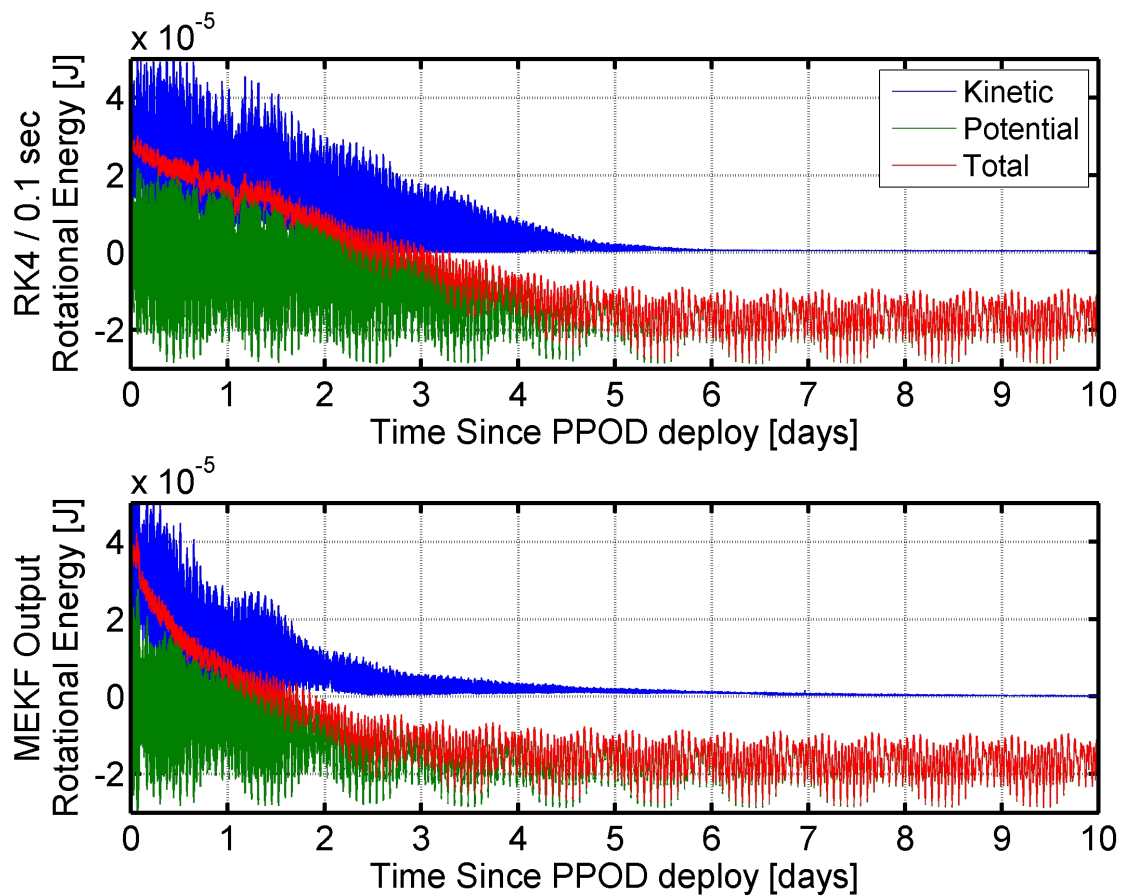


Figure 8.22: The satellite rotational kinetic (blue), potential (green), and total (black) rotational energy as simulated by the RK4 at 0.1s (top) and as measured by the MEKF output of CSSWE data (bottom).



maximum beta angle decrease is mostly linear for the simulation but less so for the filtered data.

Overall, the filtered on-orbit attitude data is in good agreement with the simulation, which is able to realistically represent the true dynamics of a PMAC system. The RK4 and RK7 settling times are 6 and 5 days after PPOD deployment; these estimates are compared to the filtered data 7.5 day settling time and are found to possess errors of 20% and 33%, respectively. The simulation performance may be compared with the RAX-2 CubeSat mission, which settled after two months despite being predicted to settle within days (see Section 3.1.3).

Simulating PMAC dynamics is difficult but the research outlined in this dissertation represents a significant step forward. It is expected that simulation performance could be improved by using a hysteresis model which is better able to represent the measured hysteresis loops over a wider range of cycle amplitudes. Even at the current simulation performance levels, the settling time estimate is quite useful for satellite mission planning purposes.

Figure 8.23: The β angle between the local magnetic field and the BZ axis as simulated by the RK4 at 0.1s (top) and as measured by the MEKF output of CSSWE data (bottom). A green line is shown marking $\beta = 10^\circ$; when the angle remains below this threshold the system is considered settled. The 3σ uncertainty bounds of the β angle are shown in red for the MEKF output dataset.

